Article

Molecular evidence of anteroposterior patterning in adult echinoderms

https://doi.org/10.1038/s41586-023-06669-2

Received: 3 February 2023

Accepted: 22 September 2023

Published online: 1 November 2023

Check for updates

L. Formery[1,2]✉, P. Peluso[3], I. Kohnle[1], J. Malnick[1], J. R. Thompson[4,5], M. Pitel[6], K. R. Uhlinger[1], D. S. Rokhsar[2,7,8,9], D. R. Rank[3,9] & C. J. Lowe[1,7,9]✉

The origin of the pentaradial body plan of echinoderms from a bilateral ancestor is one of the most enduring zoological puzzles[1,2]. Because echinoderms are defined by morphological novelty, even the most basic axial comparisons with their bilaterian relatives are problematic. To revisit this classical question, we used conserved anteroposterior axial molecular markers to determine whether the highly derived adult body plan of echinoderms masks underlying patterning similarities with other deuterostomes. We investigated the expression of a suite of conserved transcription factors with well-established roles in the establishment of anteroposterior polarity in deuterostomes[3–5] and other bilaterians[6–8] using RNA tomography and in situ hybridization in the sea star *Patiria miniata*. The relative spatial expression of these markers in *P. miniata* ambulacral ectoderm shows similarity with other deuterostomes, with the midline of each ray representing the most anterior territory and the most lateral parts exhibiting a more posterior identity. Strikingly, there is no ectodermal territory in the sea star that expresses the characteristic bilaterian trunk genetic patterning programme. This finding suggests that from the perspective of ectoderm patterning, echinoderms are mostly head-like animals and provides a developmental rationale for the re-evaluation of the events that led to the evolution of the derived adult body plan of echinoderms.

Echinoderms, defined by their calcitic endoskeleton, unique water vascular system and perhaps most strikingly by their pentaradial body plan[1,2], are among the most enigmatic animal phyla. Because echinoderms are phylogenetically nested within the deuterostomes[9,10] (echinoderms, hemichordates and chordates), their pentaradial organization was evidently derived from a bilateral ancestor. Yet, despite a rich fossil record, comparative morphological studies have come to conflicting conclusions about the axial transformations that led to pentamery from the ancestral bilaterian state[2,11]. Among bilaterians, the deployment of the gene regulatory network that specifies ectoderm anteroposterior (A–P) polarity is highly conserved[3–8] and represents a suite of characters that is often more conserved than the body plans they regulate[4,5] (Fig. 1a). The deployment of this A–P gene regulatory network could therefore provide an alternative way to test axial homology in cases such as echinoderms in which morphological characters are too divergent to reconstruct ancestral states[12].

Detailed comparisons between chordate and hemichordate axial patterning have established the exquisite conservation of the deuterostome ectodermal A–P patterning programme[4,5], which provides a phylogenetically robust framework for addressing the evolution of echinoderm axial properties. We considered two contrasting scenarios. First, the ancestral deuterostome A–P patterning network could have been dismantled and reassembled into new conformations during the radical body plan modifications along the echinoderm stem lineage. In this scenario, expression of transcription factors in derived morphological structures without extensive conservation of relative spatial expression would imply co-option into new developmental roles[13,14]. Alternatively, conservation of spatially coordinated expression of this network during the elaboration of the echinoderm adult body plan would provide a molecular basis for testing axial homology with bilaterians and establish regional homologies masked by divergent anatomies[12] (Fig. 1b).

Under the second scenario, four main proposals were made to relate the echinoderm body plan to other bilaterians that explicitly consider axial homology (Fig. 1c). The bifurcation[15] and the circularization[15,16] hypotheses can be ruled out since they require a unique molecular identity for each of the five echinoderm rays that is inconsistent with molecular data[17]. In the duplication hypothesis[15,18], each of the five echinoderm rays is a copy of the ancestral A–P axis joined anteriorly in the disk, and in the stacking hypothesis[2,11,19] the oral–aboral axis of adult echinoderms is homologous to the ancestral A–P axis. Although broad bilaterian comparisons of A–P axis patterning are typically based on ectodermal expression domains, the stacking hypothesis was proposed largely on the basis of nested posterior Hox gene expression in the posterior mesoderm of the bilateral larval stages in holothuroids (sea cucumbers), crinoids (sea lilies) and echinoids (sea urchins)[20–26]. Although initially restricted to coelomic compartments[2,19], some iterations of the stacking hypothesis have also included the oral ectoderm

[1]Department of Biology, Hopkins Marine Station, Stanford University, Pacific Grove, CA, USA. [2]Department of Molecular and Cell Biology, University of California Berkeley, Berkeley, CA, USA. [3]Pacific Biosciences, Menlo Park, CA, USA. [4]School of Biological Sciences, University of Southampton, Southampton, UK. [5]School of Ocean and Earth Science, University of Southampton, Southampton, UK. [6]Columbia Equine Hospital, Gresham, OR, USA. [7]Chan Zuckerberg BioHub, San Francisco, CA, USA. [8]Molecular Genetics Unit, Okinawa Institute of Science and Technology, Onna, Okinawa, Japan. [9]These authors contributed equally: D. S. Rokhsar, D. R. Rank, C. J. Lowe. ✉e-mail: laurent.formery@gmail.com; clowe@stanford.edu

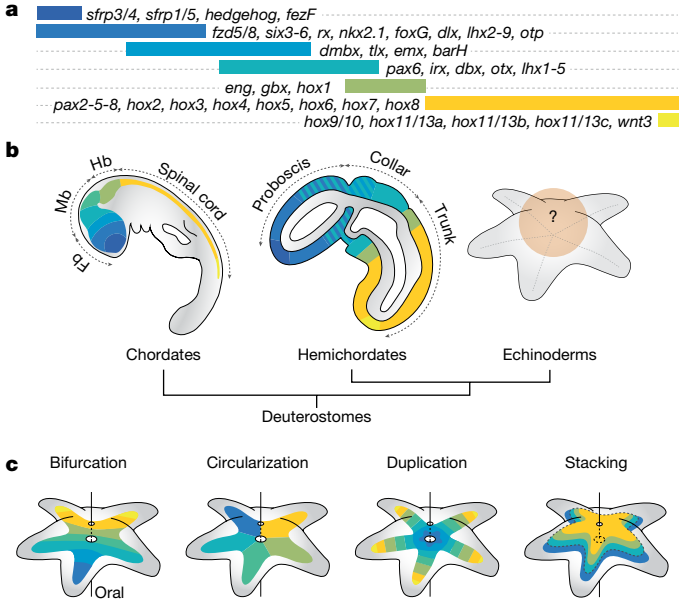

Fig. 1 | Deployment of the anteroposterior patterning system in deuterostomes. a, Expression map of the conserved transcription factors and signalling ligands involved in ectoderm patterning along the A–P axis, as observed in the hemichordate *Saccoglossus kowalevskii*. **b**, Previous work in chordates and hemichordates has demonstrated extensive regulatory conservation in ectodermal A–P patterning, establishing the ancestral regulatory characteristics of early deuterostomes. How this system is deployed in echinoderms remains unclear. **c**, Four hypotheses have been proposed for the deployment of the A–P patterning system in echinoderm adult body plan: bifurcation, circularization, duplication and stacking.

as the most anterior compartment[11]. However, recent analyses suggest that the anterior identity of the oral ectoderm should be considered independent of mesoderm derivatives[27].

Here, we tested these classical hypotheses by examining gene expression in the asteroid (sea star) *Patiria miniata* (Extended Data Fig. 1a, b), using a statistical approach based on spatial transcriptomics and in situ hybridizations. Our data provide evidence for unexpected conservation of the ancestral A–P ectodermal patterning network during ambulacrum development in juveniles. Importantly, our results do not fit with any of the established hypotheses and instead suggest a new ambulacral-anterior model to relate echinoderm pentaradial symmetry to the ancestral bilateral symmetry.

RNA tomography in adult *P. miniata*

The manifestation of pentaradial symmetry in asteroids is simpler than in other echinoderm classes because it follows a planar organization with the rays extending around the oral–aboral axis through easily distinguishable alternating ambulacral territories (where the grooves bearing the tube feet are located) and interradial territories (Fig. 2a). This makes asteroids well-suited for investigating potential axial homologies between the pentaradial echinoderm body plan and closely related bilateral deuterostomes using the molecular anatomy coordinates offered by the conserved, ectodermal A–P patterning network. The adult body plan of asteroids is defined by the endoskeleton, which underlies the body wall in the aboral and interradial areas, the digestive tract and pyloric caeca, the main body muscles, the water vascular system along each ambulacrum and the central nervous system that includes five radial nerve cords (RNC) and the circumoral nerve ring (CNR). We used microcomputed tomography (micro-CT) to show the exact spatial arrangement of the principal anatomical features in *P. miniata* juveniles along each organizational plane of the juvenile arms (Fig. 2a, Extended Data Fig. 1c,d, Supplementary Fig. 1 and Supplementary Video).

Within this anatomical framework, we began investigating the transcriptional landscape of *P. miniata* along its body axes with an unbiased spatial transcriptomics approach using RNA tomography[28]. We cryosectioned three arms from *P. miniata* juveniles at a stage that matched the micro-CT scanned specimens, along three different dimensions: from the proximal to the distal part of the arm (P–D), from the oral to the aboral side (O–A) and from the left to the right side (hereafter referred to as mediolateral; M–L) (Fig. 2b, Extended Data Fig. 1c, Supplementary Video and Supplementary Fig. 2a–c). Sections were barcoded and pooled for single-molecule real-time sequencing with PacBio IsoSeq (Supplementary Figs. 2d,e and 3a–d and Supplementary Tables 1–4), yielding a three-dimensional (3D) atlas of 25,794 gene expression profiles along the P–D, O–A and M–L dimensions of *P. miniata* arms (Fig. 2c). Gene clustering based on the similarity of RNA tomography expression profiles highlighted seven principal patterns of gene expression (Fig. 2c). We confirmed that transcriptional landscape determined by RNA tomography was consistent with the anatomy of the animal by considering principal component analyses (PCA) and Spearman correlations between sections along each dimension and analysing the expression profile of marker genes known to be expressed in specific tissues (Extended Data Fig. 1e–g). To aid in this analysis we generated a new *P. miniata* genome assembly (Supplementary Figs. 2e and 3d,e and Supplementary Tables 4 and 5).

To consider possible molecular anatomical homologies across deuterostomes we identified 36 conserved molecular markers in the RNA tomography dataset that define specific ectoderm territories along the A–P axis in hemichordates and chordates (Fig. 1a and Supplementary Fig. 4) and retrieved their expression profiles (Fig. 2d). These marker genes included transcription factors (*fezF*, *six3/6*, *nkx2.1*, *foxG*, *lhx2/9*, *otp*, *dmbx*, *tlx*, *emx*, *barH1*, *pax6*, *irx*, *dbx*, *otx*, *lhx1/5*, *engrailed*, *gbx*, *pax2/5/8*, *hox1*, *hox2*, *hox3*, *hox4*, *hox5*, *hox7*, *hox8*, *hox9/10* and *hox11/13b*), members of the Wnt signalling pathway (*sfrp1/5*, *sfrp3/4*, *fzd5/8* and *wnt3*) and the ligand *hedgehog*. Four more transcription factor markers (*rx*, *dlx*, *hox11/13a* and *hox11/13c*) were excluded from the computational analyses because of low expression levels (Supplementary Fig. 3f). *Hox6* was absent in our Hox cluster assembly (Supplementary Fig. 5), as reported previously in the closely related species *P. pectinifera*[29] and in the crown-of-thorns sea star *Acanthaster planci*[30], consistent with its loss in valvatid asteroids.

The duplication and stacking hypotheses would be supported by staggered expression of these A–P patterning markers along the P–D or O–A dimensions, respectively. We ranked the A–P patterning markers from the anterior to posterior using the hemichordate *Saccoglossus kowalevskii* as a template, as it is the most closely related bilateral species with a comprehensive expression pattern dataset for these markers (Supplementary Fig. 6). We then tested the Spearman correlation between the ranking of the genes and their position along the P–D and O–A dimensions. In both cases, we found moderate but not statistically significant correlations ($\rho = 0.25$, $P = 0.16$ and $\rho = 0.27$, $P = 0.13$, respectively) (Fig. 2e). Organizing the A–P patterning genes into seven groups on the basis of their expression profiles (Supplementary Fig. 6b), we found that the moderate correlation with the O–A dimension was mostly explained by the Hox genes alone (Fig. 2f). This was expected because the stacking hypothesis was primarily informed by the sequential expression of Hox genes in mesoderm derivatives[11,19].

Unexpectedly, we found a much stronger correlation ($\rho = 0.62$, $P = 1.4 \times 10^{-4}$) between gene order and the M–L axis (Fig. 2e). The most anterior genes appeared to be largely expressed close to the midline of the arm, whereas more posterior genes were expressed more laterally on either side of the midline. To confirm that the observed correlations were robust and not the result of sensitivity to the A–P patterning gene ranking assigned from the in situ hybridization expression data, we simultaneously shuffled the gene ranking within each of the seven

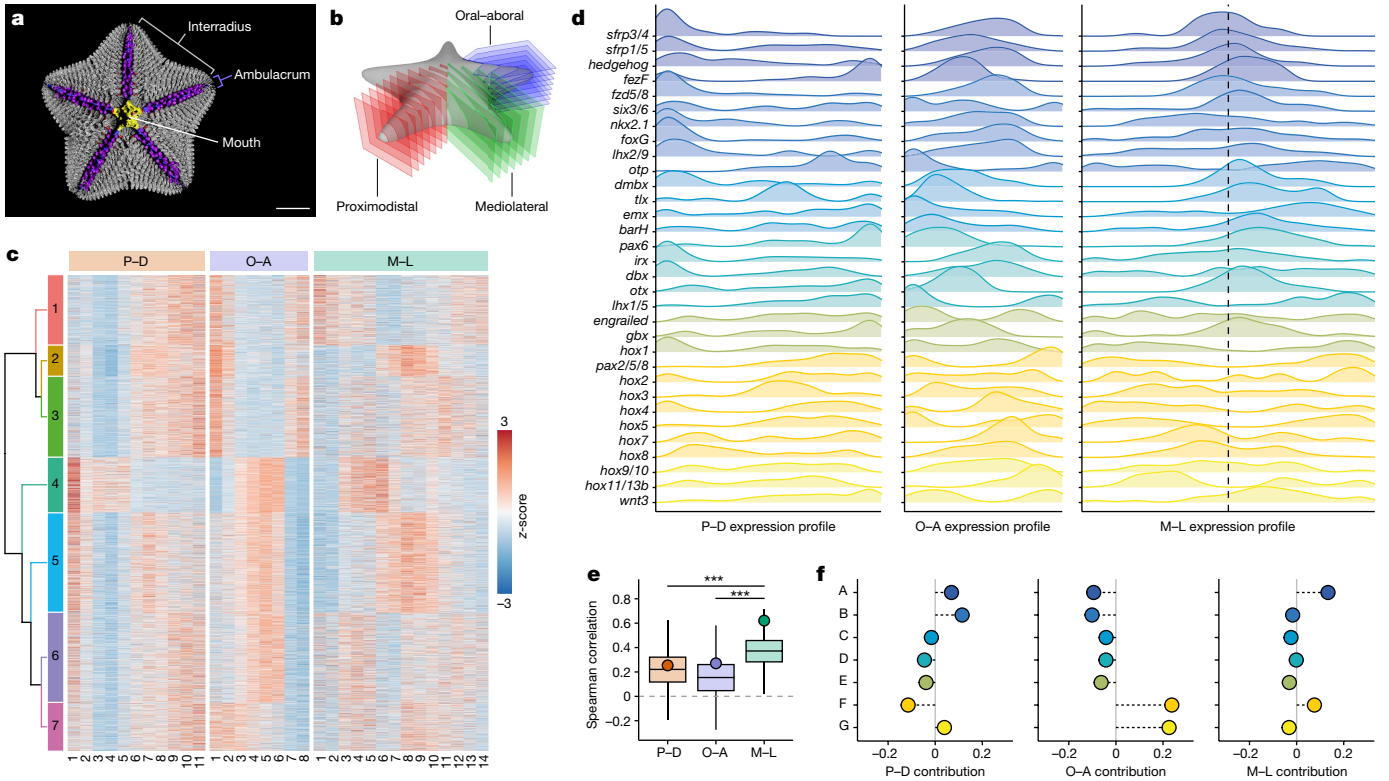

Fig. 2 | RNA tomography reveals the mediolateral dimension of the arms as the main driver of A–P patterning system deployment in *P. miniata*. **a**, Reconstructions of a young juvenile *P. miniata* scanned by micro-CT and segmented to highlight the endoskeleton (grey), the digestive tract (yellow), the main body muscles (red), the water vascular system (purple) and the central nervous system (blue). The ambulacral areas correspond to the grooves harbouring the podia and are separated by interradial areas. Scale bar, 1 mm. **b**, Experimental design of the RNA tomography with the cutting plans along the proximodistal (P–D), oral–aboral (O–A) and mediolateral (M–L) dimensions. **c**, Heatmap of gene expression *z*-scores along the P–D, O–A and M–L dimensions of the RNA tomography. **d**, Expression profiles of A–P patterning-related genes along the P–D, O–A and M–L dimensions of the RNA tomography. For the M–L dimension, the dotted line indicates the midline. Genes are ranked from the most anterior to the most posterior on the basis of their expression patterns in *Saccoglossus kowalevskii*. **e**, Spearman correlations between the ranking of the A–P patterning-related genes and their position along the three dimensions of the RNA tomography. Dots indicate the raw correlation values. Boxplots indicate the distribution of correlation values when determining the gene position along each dimension probabilistically and simultaneously shuffling the ranking of the A–P patterning-related genes for each group ($n = 10^6$ independent samples). The distribution of correlations for the M–L dimension is significantly higher than for the P–D and O–A dimensions (two-sided Wilcoxon rank test; $P < 10^{-4}$). Centre lines, median; box, interquartile range (IQR); whiskers, highest and lowest values at ±1.5× IQR. **f**, Relative contribution of each group of A–P patterning-related genes to the Spearman correlation between the ranking of the A–P patterning-related genes and their position along the three dimensions of the RNA tomography.

groups and probabilistically sampled the position for each gene, using the expression *z*-score as a law of probability, in 10^6 replications. For all the simulated replications, the distribution of M–L correlations was significantly superior to the P–D and O–A correlations, with a two-sided Wilcoxon rank test *P*-value inferior to 10^{-4} in both cases (Fig. 2e). This suggested that neither the duplication nor the stacking hypotheses accurately describe the deployment of A–P-related patterning genes in *P. miniata* and that most of the underlying patterning logic of the pentaradial plan is not explained by existing models.

M–L deployment of A–P patterning genes

Although RNA tomography provides coarse average axial positional information, these patterns cannot be directly linked to germ layers or anatomical structures. To investigate axial patterning in more detail, we examined the expression pattern of the 36 marker genes using in situ hybridization chain reactions (HCRs; Supplementary Fig. 7) on postmetamorphic juveniles. This representative stage follows the resorption of larval structures into the rudiment during metamorphosis (Fig. 3a). The elaboration of the pentaradial symmetry is initiated earlier within the larval mesoderm but the mechanistic basis of this process is probably distinct from those that give their regional identity to the final axes of the pentaradial body plan. Expression of classical ectoderm A–P patterning genes such as *six3/6*, *nkx2.1*, *dmbx*, *pax6* and *otx* was initiated at low levels in the presumptive adult tissues at the onset of metamorphosis but only reached robust levels of expression which were relatable to ambulacral polarity in postmetamorphic juveniles, when the definitive adult body plan is elaborated (Fig. 3b and Supplementary Fig. 8). We focused on early juvenile stages as a readout of early establishment of axial patterning. As in the adult, the juvenile body plan is organized into ambulacral territories on the oral side and interradial territories at the edge of the ambulacra and extending around to envelop the entire aboral side. The ambulacral ectoderm is divided in two main regions: the medial ambulacral ectoderm comprising the RNCs and the CNR and more laterally the epidermis covering the podia (Fig. 3c,d).

We analysed the expression of four groups of patterning genes expressed along the A–P axis in both hemichordates and chordates. The first group (*fzd5/8*, *nkx2.1*, *rx*, *sfrp1/5*, *foxG*, *six3/6* and *hedgehog*) has strong anterior ectodermal localization in the proboscis of *S. kowalevskii*[4,5] and in the forebrain of vertebrates[31,32] (Fig. 1a,b). In *P. miniata* we found similarly overlapping patterns of regional expression, mostly restricted to the developing CNR, the RNCs and, in the case of *six3/6* and *hedgehog*, in repeated domains where lateral nerves from the RNCs

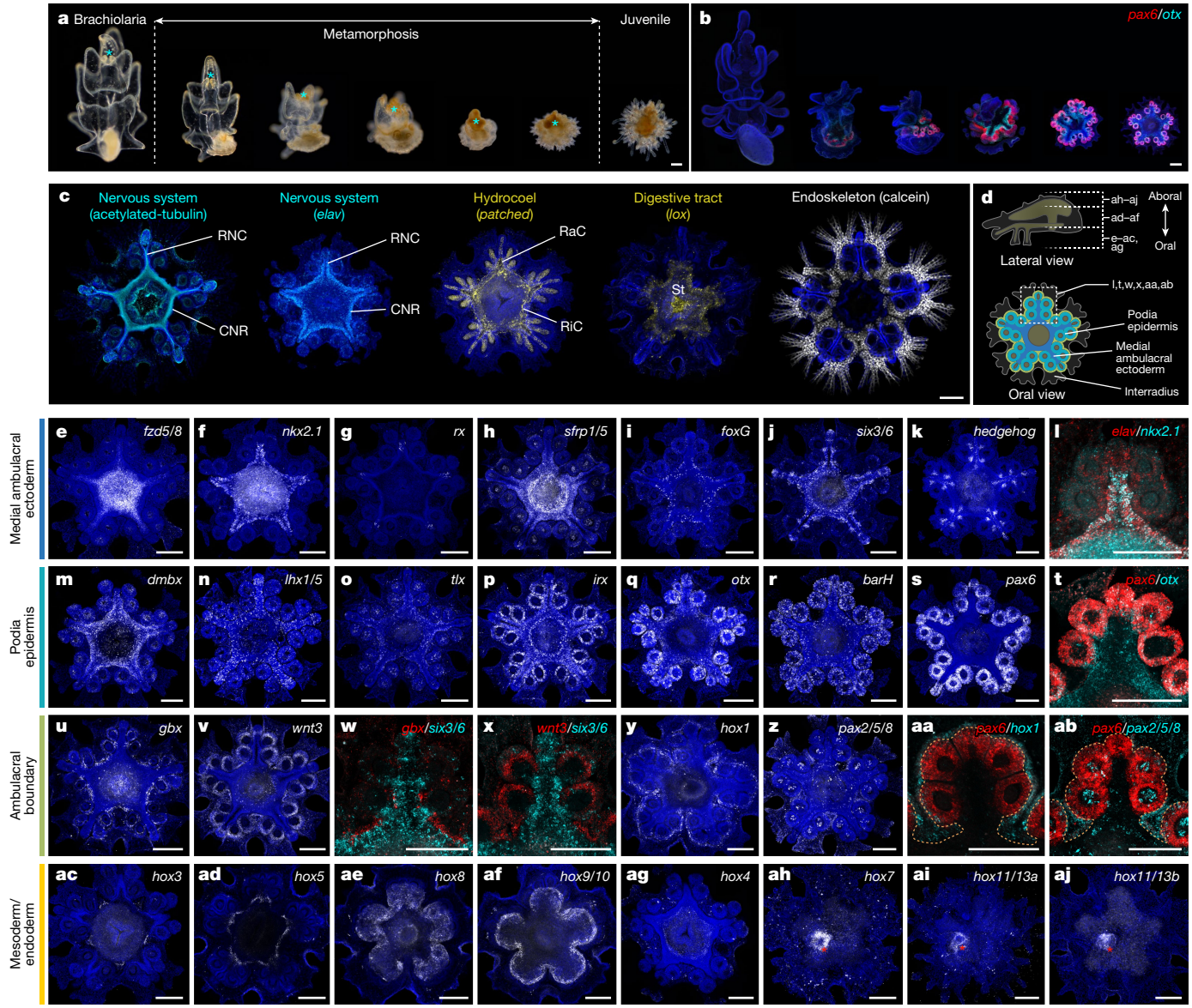

Fig. 3 | Gene expression data reveal the deployment of the A–P patterning system in *P. miniata* ambulacral ectoderm. a, Metamorphosis in *P. miniata*. The anterior part of the brachiolaria larva (cyan asterisk) is resorbed into the rudiment. **b**, HCRs showing *pax6* (red) and *otx* (cyan) starting to be expressed during metamorphosis in the developing adult pentaradial body plan. Specimens are counterstained with DAPI (blue). **c**, Main anatomical features of postmetamorphic juveniles, imaged from the oral side: the nervous system (cyan) stained with antibodies against acetylated tubulin highlighting the nerve tracts and the neuronal marker *elav* highlighting the cell bodies, the hydrocoel (yellow) stained with the marker *patched*, the digestive tract (yellow) stained with the marker *lox* and the endoskeleton (white) stained using calcein. Specimens are counterstained with DAPI (blue). RNC, radial nerve cord; CNR, circumoral nerve ring; RaC, radial canal; RiC, ring canal; St, stomach **d**, Schematics showing the oral–aboral position of the HCR *z*-projections shown in **e**–**aj** (top) and the main anatomical regions visible on the postmetamorphic juveniles oral side (bottom). The white square on the bottom panel indicates the position of the close-ups in **l**,**t**,**w**,**x**,**aa**,**ab**. **e**–**aj**, HCRs of *P. miniata* juveniles imaged from the oral side (**e**–**ag**) or the aboral side (**ah**–**aj**). In **e**–**k**,**m**–**s**,**u**,**v**,**y**,**z**,**ac**–**aj**, specimens are counterstained with DAPI (blue). **l**,**t**,**w**,**x**,**aa**,**ab**, magnification of a single ambulacrum. **e**–**l**, Genes primarily expressed in the medial ambulacral ectoderm. Colocalization with *elav* indicates expression in the CNR and the RNCs. **m**–**t**, Genes primarily expressed in the podia epidermis. **u**–**ab**, Genes primarily expressed in the ambulacral boundary. In **aa**,**ab**, orange dotted lines outline the ambulacral ectoderm. **ac**–**af**, Hox genes primarily expressed in the coeloms. **ag**–**aj**, Hox genes primarily expressed in the digestive tract. In **ah**–**aj**, red asterisks indicate the position of the developing intestinal tract. Scale bars, 100 µm.

connect with each pair of secondary podia (Fig. 3e–l and Supplementary Fig. 9a–e). This region corresponded to the most medial part of the ambulacral ectoderm (Fig. 3d). These findings are inconsistent with the duplication hypothesis, which predicts a staggered expression of anterior to posterior markers along each RNC.

The next group (*lhx1/5*, *dmbx*, *tlx*, *irx*, *fezF*, *dbx*, *otx*, *barH* and *pax6*) overlaps with the previous anterior-class genes in *S. kowalevskii* but with a more caudal distribution in the posterior proboscis and into the collar[4]; in chordates, these genes are primarily expressed either in the forebrain or the midbrain[3,31] (Fig. 1a,b). In *P. miniata*, expression of this group of genes overlaps in the most medial territory with the most anterior-class genes but with expanded lateral domains on either side of the RNCs (Fig. 3d,m–s and Supplementary Fig. 9f–h), into the epidermis covering the podia. *FezF* and *dbx* were only expressed in a few cells in the ambulacral ectoderm (Supplementary Fig. 10a–c). Only *pax6* was not expressed in the medial ambulacral ectoderm and was restricted to the podia epidermis, as previously reported in other echinoderm species[33,34] (Fig. 3t). Thus, the lateral ambulacral ectoderm

appears to have a more posterior molecular identity, similar to that of the hemichordate collar or the vertebrate midbrain.

The third category (*gbx*, *wnt3*, *hox1* and *pax2/5/8*) includes genes that have more posterior expression patterns in hemichordates and chordates (Fig. 1a,b). *Gbx*, *hox1* and *pax2/5/8* are all expressed in hemichordates in the anterior trunk, close to the boundary with the collar, and in chordates in the hindbrain and into the midbrain/hindbrain boundary[5,35,36]. *Wnt3* is expressed at the far posterior end of the A–P axis in both phyla[37,38]. In *P. miniata*, we found that these four genes are expressed at the boundary between the ambulacral ectoderm and the interradial territory (Fig. 3d,u–ab and Supplementary Fig. 9i–l). *Gbx* and *wnt3* were expressed in the outer part of the ambulacral ectoderm, establishing a mutually exclusive boundary with more anterior genes like *six3/6* (Fig. 3u–x). *Hox1* and *pax2/5/8* were expressed more laterally compared to *gbx* and *wnt3*; *hox1* outlined the entire ambulacral area, whereas *pax2/5/8* had a more complex expression pattern and was primarily expressed between the ambulacra (Fig. 3y–ab). We suggest that in *P. miniata* these genes marked the outer limit of an anterior compartment.

Finally, Hox genes are expressed in hemichordates and chordates posteriorly to the collar/trunk and midbrain/hindbrain boundary, respectively, and are involved in trunk patterning[4,35,39] (Fig. 1a,b). In *P. miniata*, only *hox1* was detected in the ectoderm. *Hox3*, *hox5*, *hox8* and *hox9/10* were expressed in mesoderm derivatives (Fig. 3ac–af). *Hox4* expression was barely above the detection threshold but was found in the pharynx (Fig. 3ag), whereas *hox7*, *hox11/13a* and *hox11/13b* were expressed in the developing intestinal tract (Fig. 3ah–aj). These observations are in line with previous reports that Hox expression in echinoderms is largely restricted to internal germ layers[20–26] and consistent with the Hox-driven O–A correlation observed in our RNA tomography dataset. In hemichordates and other bilaterians, Hox gene domains are intercalated during trunk development between the anterior domains and the posterior end of the animal, which expresses posteriorizing factors such as *wnt3* (ref. 35,40). We propose that there is no ectoderm equivalent to a trunk region in *P. miniata* because *wnt3* is expressed at the edge of the ambulacral region and because *hox1* is the only Hox gene expressed in the ectoderm. Therefore, the deployment of the A–P patterning system in *P. miniata* seems to be limited to the ambulacral region and its boundary.

We also found that in *P. miniata* some ancestral deuterostome A–P patterning genes did not exhibit conserved relative expression compared to hemichordates and vertebrates, either because they were not detected (*dlx*), not expressed in the ectoderm (*engrailed* and *sfrp3/4*) or exhibited different relative spatial arrangements (*lhx2/9*, *emx* and *otp*) (Supplementary Fig. 10d–i). Some well-established boundaries in hemichordates and vertebrates like the abutting *otx* and *gbx* domains were also not observed in *P. miniata*. This presumably reflects the plasticity of the A–P patterning system and its adaptation to the radically different pentaradial body plan. Despite these discrepancies, germ-layer-specific expression patterns corroborated that the M–L dimension revealed by RNA tomography was the main and unexpected driver of the ectoderm A–P patterning logic of the pentaradial body plan in *P. miniata*.

If the ancestral deuterostome A–P patterning system is used to remodel the sea star body plan at metamorphosis, are other correlated bilaterian axial patterning systems contributing to the patterning of the adult body plan as well? In bilaterians, the dorsoventral (D–V) axis is specified transiently during embryogenesis by conserved BMP2/4 and Chordin gradients[41,42]. Later on, the neuroectoderm and mesoderm derivatives are patterned along the D–V axis via the deployment of transcription factors such as *pax3/7*, *msx* and *tbx2/3* in response to BMP signalling[43–45] (Extended Data Fig. 2a). To investigate whether the BMP/Chordin axis is involved in the formation of the adult body plan in *P. miniata*, we first looked at the expression of genes involved in D–V axis specification through metamorphosis and in postmetamorphic juveniles (Extended Data Fig. 2b–s and Supplementary Fig. 4). Although *chordin* was not detected by in situ hybridization, we found that *BMP2/4*, *BMP1* and *ADMP1* were consistently expressed in the distal part of the developing tube feet mesoderm, starting early during metamorphosis and into the juvenile (Extended Data Fig. 2c–s). In addition, we looked at known target genes of BMP signalling (Extended Data Fig. 2b,t–v and Supplementary Fig. 4). Although *pax3/7* is lost in echinoderms[46], *tbx2/3* and *msx* were co-expressed with *BMP2/4* in the tube feet and *tbx2/3* also expressed in the overlying tube feet ectoderm, suggesting a similar relationship to BMP signalling to that previously demonstrated in vertebrates (Extended Data Fig. 2t–v). These expression data are consistent with previous studies from a direct-developing echinoid[47] and support a role for BMP signalling in tube feet development, more equivalent to the later role of BMP in dorsal midline patterning in hemichordates and vertebrates[43,48]. However, our results do not indicate BMP/Chordin signalling as defining an anatomical axis in the pentaradial body plan of *P. miniata*.

Echinoderm rays have also been proposed to be homologous to bilaterian appendages[49,50]. In principle, this scenario could be compatible with our expression data, with the rays being appendages of an anterior territory. To assess this possibility, we considered conserved markers for P–D appendage development, which involves polarized expression of *meis*, *pbx*, *dlx* and *sp8-9* in vertebrates, arthropods and cephalopods[51] (Extended Data Fig. 2w,x and Supplementary Fig. 4). Although we found the expression of *Pbx* and particularly *sp8-9* to be compatible with this idea, *dlx* was not detected and *meis* had an inconsistent expression domain (Extended Data Fig. 2x–α). The extension of the echinoderm ambulacra probably involves substantial developmental novelty. The RNA tomography dataset will be an invaluable resource for hypothesis generation and identification of candidate genes to form the basis of a more in depth developmental investigations of this process.

Evolution of axial properties in echinoderms

The organizational modifications to the ancestral bilateral deuterostome body plan during early echinoderm evolution are so profound that even basic axial comparisons with other deuterostome taxa have been problematic at the morphological level[2]. Here, we investigated this fundamental question by spatially mapping the deployment of the ancestral bilaterian ectodermal A–P patterning system in the pentaradial body plan of *P. miniata*. Because this patterning system is largely conserved between hemichordates and chordates, we can confidently reconstruct its ancestry in early deuterostomes and at the base of ambulacrarians[4,5].

We found that that much of the ancestral anterior patterning network is spatially deployed in a manner incompatible with previously proposed hypotheses of echinoderm axial homologies[11,15]. Rather, expression patterns map onto a new coordinate system which we call the 'ambulacral-anterior' model of echinoderm body plan evolution (Fig. 4a,b). In this model, the midline of each ambulacrum expresses the most anterior bilaterian molecular identity, equivalent to the forebrain and proboscis in vertebrates and hemichordates, respectively. The midlateral regions on either side of the nerve cords, including the ectoderm wrapping the podia, share patterning similarities with more caudal ectodermal territories of hemichordates and chordates, down to the collar and midbrain, respectively. Finally, the boundary at the edge of the ambulacral ectoderm displays the most posterior molecular profile corresponding to the collar/trunk boundary of hemichordates and the midbrain/hindbrain boundary of vertebrates. According to our ambulacral-anterior model, echinoderms are the first example of bilaterians in which the 'anterior' identity is located at the centre of a sheet of tissue, rather than being located at an extremity. The anatomical outputs of this anterior domain, however, share similarities across all deuterostome phyla (including echinoderms) in that they include neural condensations and an extensive array of sensory structures.

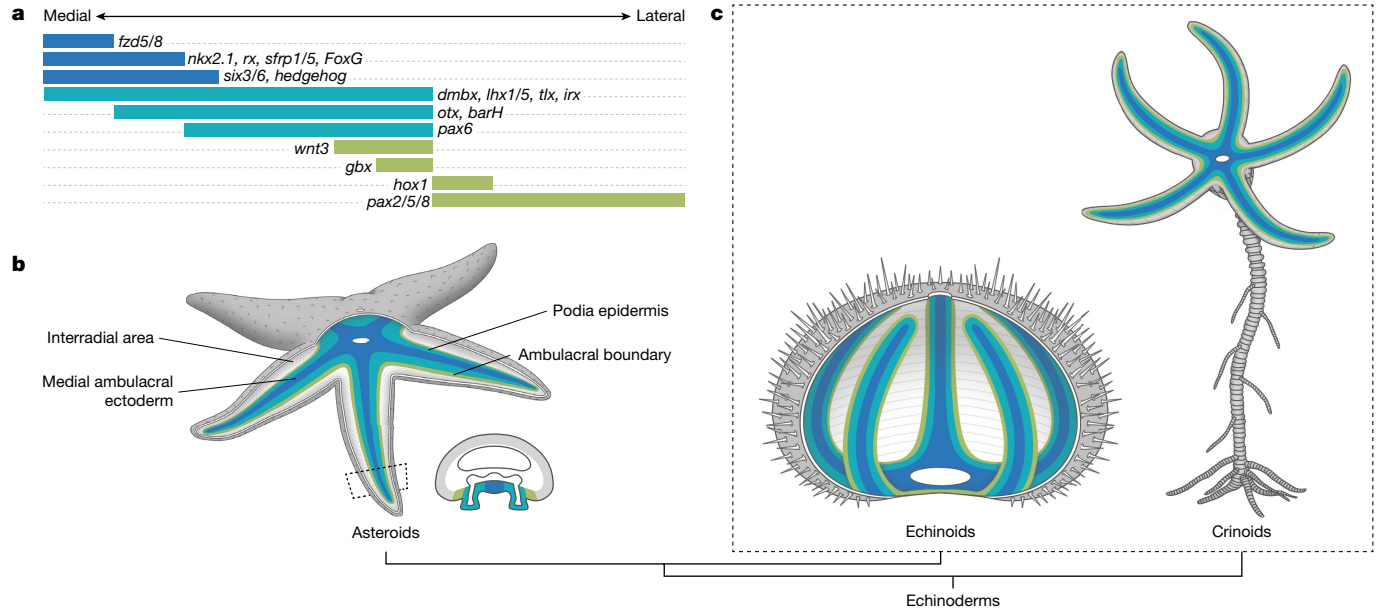

Fig. 4 | The ambulacral-anterior model of echinoderm body plan evolution. **a**, Expression map of the conserved transcription factors and signalling ligands involved in the ambulacral ectoderm patterning in *P. miniata*, organized from the midline of the ambulacrum (left) towards the interradius (right). **b**, Diagram of the ambulacral-anterior model in a generalized asteroid. Anterior patterning genes are expressed in the oral ambulacral ectoderm, shown through a cut-away of the forward part of the animal and a cross-section through the forward arm. Only genes expressed in the ectoderm are shown. **c**, Ambulacral-anterior model applied to echinoderm classes with available gene expression data, echinoids (left) and crinoids (right). In echinoids, the ambulacral ectoderm is internalized and shown through a cut-away of the forward part of the test, whereas in crinoids the ambulacral ectoderm is embedded in the oral epidermis, similar to asteroids.

Strikingly, despite the presence of a genomic Hox cluster, ectodermal Hox gene expression is largely absent in the sea star (except for *hox1*), suggesting a loss of the ancestral ectodermal trunk regulatory programme, which is consistent with previous observations in the echinoid *Peronella japonica*[27]. Yet, Hox genes are expressed in the mesoderm and endoderm, displaying a marked uncoupling of germ-layer A–P patterning as recognized previously[27,52]. The mesoderm and endoderm trunk programmes are wrapped in an ectoderm with two clear territories, including (1) an ambulacral-anterior-like domain that is the main focus of our work and unexpectedly (2) an extensive interradial domain that extends around the aboral side of the animal and displays uncertain axial identity, without any detectable readout of the ancestral A–P patterning programme, as previously observed in echinoids[27]. The uncoupling of an ectodermal head and trunk programmes is not unique to *P. miniata* and has been demonstrated in both larval echinoderms and hemichordates[35,53] and more recently in protostome larvae[40,54], suggesting that these regulatory programmes can be uncoupled over macro-evolutionary time frames.

Previous studies[13,14] proposed that the deployment of transcription factors to pattern adult echinoderm body plans could be the result of co-option, meaning recruitment of an existing gene or regulatory module (or duplication thereof) to fulfil a new developmental role[55]. Here, using a much larger set of genes, we demonstrate that the patterning of the ambulacral ectoderm in *P. miniata* involves a collection of interacting modules that define distinct regions along the A–P axis of bilateral animals rather than a single regulatory programme. Co-option of this network would require redeployment of these interacting modules into a new role in stem echinoderms. Thus, although we acknowledge that co-option remains a possible scenario, we propose that the observed pattern in extant asteroid ambulacra is a result of modification of an ancestral deuterostome axial programme during echinoderm evolution. Documented cases of co-option such as the deployment of posterior Hox genes during limb patterning[56] involve the (re)use of an existing regulatory network to pattern a new structure, without affecting the ancestral role of the system. To our knowledge there is no example of co-option that involves dismantling of the ancestral patterning networks following their recruitment into the development of a new structure. A co-option scenario in echinoderms would imply that the ancestral function of the A–P patterning network was lost in the adult body plan, after co-option into an evolving ambulacral territory, which in our opinion is less parsimonious than proposing descent with modification of an ancestral A–P axis. Interestingly, a route to resolve this issue might come from some interpretations of homalozoan and helicoplacoid echinoderms that propose these groups to be transitional forms between bilateral and pentaradial symmetry[57]. Re-interpreting these fossils in light of new patterning datasets could allow us to discriminate between co-option with loss of the ancestral axial registry or descent with modification.

Did the reorganization of the ancestral A–P axis documented here occur during the early stem evolution of echinoderms as a defining regulatory feature of crown group echinoderms or during the later diversification of asteroids? Our model inferred from analysis of asteroid data is consistent with published findings from two other main echinoderm clades, crinoids and echinoids. In crinoids, the expression of *six3/6*, *otx* and *pax6* has been reported in the ambulacral ectoderm[58]. In echinoids, A–P patterning-related genes have been surveyed in various species including *Strongylocentrotus purpuratus* and *Heliocidaris erythrogramma*[20,33,34] and most extensively in *P. japonica*[25,27] in which the anterior identity of the ambulacral ectoderm was already reported[27]. In both crinoids and echinoids, most of the anterior patterning-related genes studied show expression patterns compatible with the ambulacral-anterior model. Furthermore, Hox gene expression has been described in echinoids, holothuroids and crinoids[20–26] and is also largely congruent with the expression patterns that we observed in *P. miniata*. This suggests that on the basis of limited available comparative data, the ambulacral-anterior model could be a general developmental feature of all extant echinoderm classes and that our observations reflect early regulatory changes which occurred during stem echinoderm evolution (Fig. 4c). Further comprehensive comparative analyses will be required to test this hypothesis.

The evolution of body plan variations across echinoderm classes has proven challenging to reconstruct on the basis of morphological features alone[59]. The ambulacral-anterior model offers a powerful tool to establish robust regional homologies between echinoderm classes. Most importantly, the new axial paradigm established here can be integrated with the exquisite fossil record of the phylum to reinvestigate key morphological transformations in light of regulatory changes.

Online content

Any methods, additional references, Nature Portfolio reporting summaries, source data, extended data, supplementary information, acknowledgements, peer review information; details of author contributions and competing interests; and statements of data and code availability are available at https://doi.org/10.1038/s41586-023-06669-2.

1. Hyman, L. H. *The Invertebrates, Vol. IV, Echinodermata: The Coelomate Bilateria* (McGraw-Hill, 1955).
2. Smith, A. B. Deuterostomes in a twist: the origins of a radical new body plan. *Evol. Dev.* **10**, 493–503 (2008).
3. Albuixech-Crespo, B. et al. Molecular regionalization of the developing amphioxus neural tube challenges major partitions of the vertebrate brain. *PLoS Biol.* **15**, e2001573 (2017).
4. Lowe, C. J. et al. Anteroposterior patterning in hemichordates and the origins of the chordate nervous system. *Cell* **113**, 853–865 (2003).
5. Pani, A. M. et al. Ancient deuterostome origins of vertebrate brain signalling centres. *Nature* **483**, 289–294 (2012).
6. Reichert, H. & Simeone, A. Developmental genetic evidence for a monophyletic origin of the bilaterian brain. *Philos. Trans. R. Soc. Lond. B* **356**, 1533–1544 (2001).
7. Hirth, F. et al. An urbilaterian origin of the tripartite brain: developmental genetic insights from *Drosophila*. *Development* **130**, 2365–2373 (2003).
8. Tomer, R., Denes, A. S., Tessmar-Raible, K. & Arendt, D. Profiling by image registration reveals common origin of annelid mushroom bodies and vertebrate pallium. *Cell* **142**, 800–809 (2010).
9. Bromham, L. D. & Degnan, B. M. Hemichordates and deuterostome evolution: robust molecular phylogenetic support for a hemichordate+echinoderm clade. *Evol. Dev.* **1**, 166–171 (1999).
10. Cameron, C. B., Garey, J. R. & Swalla, B. J. Evolution of the chordate body plan: new insights from phylogenetic analyses of deuterostome phyla. *Proc. Natl Acad. Sci. USA* **97**, 4469–4474 (2000).
11. David, B. & Mooi, R. How Hox genes can shed light on the place of echinoderms among the deuterostomes. *EvoDevo* **5**, 22 (2014).
12. Lowe, C. J., Clarke, D. N., Medeiros, D. M., Rokhsar, D. S. & Gerhart, J. The deuterostome context of chordate origins. *Nature* **520**, 456–465 (2015).
13. Lowe, C. J. & Wray, G. A. Radical alterations in the roles of homeobox genes during echinoderm evolution. *Nature* **389**, 718–721 (1997).
14. Li, Y. et al. Genomic insights of body plan transitions from bilateral to pentameral symmetry in Echinoderms. *Com. Biol.* **3**, 371 (2020).
15. Popodi, E.,Andrews, M. & Raff, R. A. Evolution of body plans: using homeobox genes to examine the development of the radial CNS of echinoderms. *Dev. Biol.* **163**, 540 (1994).
16. Rozhnov, S. V. Symmetry of echinoderms: from initial bilaterally-asymmetric metamerism to pentaradiality. *Nat. Sci.* **6**, 171–183 (2014).
17. Holland, L. Z. Evolution of basal deuterostome nervous systems. *J. Exp. Biol.* **218**, 637–645 (2015).
18. Byrne, M., Martinez, P. & Morris, V. Evolution of a pentameral body plan was not linked to translocation of anterior Hox genes: the echinoderm HOX cluster revisited. *Evol. Dev.* **18**, 137–143 (2016).
19. Peterson, K. J., Arenas-Mena, C. & Davidson, E. H. The A/P axis in echinoderm ontogeny and evolution: evidence from fossils and molecules. *Evol. Dev.* **2**, 93–101 (2000).
20. Arenas-Mena, C., Cameron, A. R. & Davidson, E. H. Spatial expression of Hox cluster genes in the ontogeny of a sea urchin. *Development* **127**, 4631–4643 (2000).
21. Morris, V. B. & Byrne, M. Involvement of two Hox genes and Otx in echinoderm body-plan morphogenesis in the sea urchin *Holopneustes purpurescens*. *J. Exp. Zool. B Mol.* **304**, 456–467 (2005).
22. Hara, Y. et al. Expression patterns of Hox genes in larvae of the sea lily *Metacrinus rotundus*. *Dev. Genes Evol.* **216**, 797–809 (2006).
23. Cisternas, P. & Byrne, M. Expression of Hox4 during development of the pentamerous juvenile sea star, *Parvulastra exigua*. *Dev. Genes Evol.* **219**, 613–618 (2009).
24. Morris, V. B. & Byrne, M. Oral–aboral identity displayed in the expression of HpHox3 and HpHox11/13 in the adult rudiment of the sea urchin *Holopneustes purpurescens*. *Dev. Genes Evol.* **224**, 1–11 (2014).
25. Tsuchimoto, J. & Yamaguchi, M. Hox expression in the direct-type developing sand dollar *Peronella japonica*. *Dev. Dynam.* **243**, 1020–1029 (2014).
26. Kikuchi, M., Omori, A., Kurokawa, D. & Akasaka, K. Patterning of anteroposterior body axis displayed in the expression of Hox genes in sea cucumber *Apostichopus japonicus*. *Dev. Genes Evol.* **225**, 275–286 (2015).
27. Adachi, S. et al. Anteroposterior molecular registries in ectoderm of the echinus rudiment. *Dev. Dynam.* **247**, 1297–1307 (2018).
28. Junker, J. P. et al. Genome-wide RNA tomography in the zebrafish embryo. *Cell* **159**, 662–675 (2014).
29. Tominaga, H., Nishitsuji, K. & Satoh, N. A single-cell RNA-seq analysis of early larval cell-types of the starfish, *Patiria pectinifera*: insights into evolution of the chordate body plan. *Dev. Biol.* **496**, 52–62 (2023).
30. Baughman, K. W. et al. Genomic organization of Hox and Para Hox clusters in the echinoderm, *Acanthaster planci*. *Genesis* **52**, 952–958 (2014).
31. Shimamura, K., Hartigan, D. J., Martinez, S., Puelles, L. & Rubenstein, J. L. Longitudinal organization of the anterior neural plate and neural tube. *Development* **121**, 3923–3933 (1995).
32. Quinlan, R., Graf, M., Mason, I., Lumsden, A. & Kiecker, C. Complex and dynamic patterns of Wnt pathway gene expression in the developing chick forebrain. *Neural Dev.* **4**, 35 (2009).
33. Byrne, M. et al. Expression of genes and proteins of the pax-six-eya-dach network in the metamorphic sea urchin: insights into development of the enigmatic echinoderm body plan and sensory structures. *Dev. Dynam.* **247**, 239–249 (2018).
34. Paganos, P. et al. New model organism to investigate extraocular photoreception: opsin and retinal gene expression in the sea urchin *Paracentrotus lividus*. *Cells* **11**, 2636 (2022).
35. Gonzalez, P., Uhlinger, K. R. & Lowe, C. J. The adult body plan of indirect developing hemichordates develops by adding a Hox-patterned trunk to an anterior larval territory. *Curr. Biol.* **27**, 87–95 (2017).
36. Wurst, W. & Bally-Cuif, L. Neural plate patterning: upstream and downstream of the isthmic organizer. *Nat. Rev. Neuro.* **2**, 99–108 (2001).
37. Darras, S. et al. Anteroposterior axis patterning by early canonical Wnt signaling during hemichordate development. *PLoS Biol.* **16**, e2003698 (2018).
38. Liu, P. et al. Requirement for Wnt3 in vertebrate axis formation. *Nat. Genet.* **22**, 361–365 (1999).
39. Krumlauf, R. et al. Hox homeobox genes and regionalisation of the nervous system. *J. Neurobiol.* **24**, 1328–1340 (1993).
40. Martín-Zamora, F. M. et al. Annelid functional genomics reveal the origins of bilaterian life cycles. *Nature* **615**, 105–110 (2023).
41. Holley, S. A. et al. A conserved system for dorsal–ventral patterning in insects and vertebrates involving *sog* and *chordin*. *Nature* **376**, 249–253 (1995).
42. De Robertis, E. M. & Sasai, Y. A common plan for dorsoventral patterning in Bilateria. *Nature* **380**, 37–40 (1996).
43. Lee, K. J. & Jessell, T. M. The specification of dorsal cell fates in the vertebrate central nervous system. *Annu. Rev. Neurosci.* **22**, 261–294 (1999).
44. Yamada, M., Revelli, J. P., Eichele, G., Barron, M. & Schwartz, R. J. Expression of chick *Tbx-2*, *Tbx-3* and *Tbx-5* genes during early heart development: evidence for BMP2 induction of *Tbx2*. *Dev. Biol.* **228**, 95–105 (2000).
45. Timmer, J. R., Wang, C. & Niswander, L. BMP signaling patterns the dorsal and intermediate neural tube via regulation of homeobox and helix-loop-helix transcription factors. *Development* **129**, 2459–2472 (2002).
46. Barton-Owen, T. B., Ferrier, D. E. & Somorjai, I. M. *Pax3/7* duplicated and diverged independently in amphioxus, the basal chordate lineage. *Sci Rep.* **8**, 9414 (2018).
47. Koop, D. et al. Nodal and BMP expression during the transition to pentamery in the sea urchin *Heliocidaris erythrogramma*: insights into patterning the enigmatic echinoderm body plan. *BMC Dev. Biol.* **17**, 4 (2017).
48. Lowe, C. J. et al. Dorsoventral patterning in hemichordates: insights into early chordate evolution. *PLoS Biol.* **4**, e291 (2006).
49. Panganiban, G. et al. The origin and evolution of animal appendages. *Proc. Natl Acad. Sci. USA* **94**, 5162–5166 (1997).
50. Hotchkiss, F. H. A "rays-as-appendages" model for the origin of pentamerism in echinoderms. *Paleobiology* **24**, 200–214 (1998).
51. Tarazona, O. A., Lopez, D. H., Slota, L. A. & Cohn, M. J. Evolution of limb development in cephalopod mollusks. *eLife* **8**, e43828 (2019).
52. Lacalli, T. Echinoderm conundrums: Hox genes, heterochrony and an excess of mouths. *EvoDevo* **5**, 46 (2014).
53. Yankura, K. A., Martik, M. L., Jennings, C. K. & Hinman, V. F. Uncoupling of complex regulatory patterning during evolution of larval development in echinoderms. *BMC Biol.* **8**, 143 (2010).
54. Gąsiorowski, L. & Hejnol, A. Hox gene expression during development of the phoronid *Phoronopsis harmeri*. *EvoDevo* **11**, 2 (2020).
55. True, J. R. & Carroll, S. B. Gene co-option in physiological and morphological evolution. *Annu. Rev. Cell Dev. Biol.* **18**, 53–80 (2002).
56. Zákány, J. & Duboule, D. Hox genes in digit development and evolution. *Cell Tissue Res.* **296**, 19–25 (1999).
57. Smith, A. B. & Zamora, S. Cambrian spiral-plated echinoderms from Gondwana reveal the earliest pentaradial body plan. *Proc. R. Soc. B* **280**, 20131197 (2013).
58. Omori, A., Shibata, T. F. & Akasaka, K. Gene expression analysis of three homeobox genes throughout early and late development of a feather star *Anneissia japonica*. *Dev. Genes Evol.* **230**, 305–314 (2020).
59. Zamora, S. & Rahman, I. A. Deciphering the early evolution of echinoderms with Cambrian fossils. *Paleontology* **57**, 1105–1119 (2014).

Publisher's note Springer Nature remains neutral with regard to jurisdictional claims in published maps and institutional affiliations.

Springer Nature or its licensor (e.g. a society or other partner) holds exclusive rights to this article under a publishing agreement with the author(s) or other rightsholder(s); author self-archiving of the accepted manuscript version of this article is solely governed by the terms of such publishing agreement and applicable law.

© The Author(s), under exclusive licence to Springer Nature Limited 2023

Methods

Animal husbandry and tissue preparation

All animal collection and handling was in compliance with US ethical regulations. Adult and young (~1–2 cm wide) *P. miniata* specimens were collected off the coast of Monterey Bay, California, United States, and kept in circulating seawater tanks. Young specimens were used for X-ray micro-CT, extract genomic DNA (gDNA) and RNA tomography (see below). For RNA tomography datasets and gDNA, two young specimens of the same class of size as those used for micro-CT (referred to as specimens 1 and 2) were used. They were anaesthetized in filtered seawater and 7.5% MgCl (1:1) and then four arms were dissected out. One of the arms was proceeded for DNA extraction and the three others were included in HistoPrep embedding medium (ThermoFischer). Finally, to generate fixed material for HCRs and immunochemistry (see below), several batches of gravid adults were spawned by injecting 1 ml of 1 µM 1-methyladenine (Acros Organics) in each of the gonads. Sperm and mature oocytes were released by the animals about 45 and 90 min after the injection, respectively. Following in vitro fertilization, embryos were cultured at 14 °C in ultraviolet-sterilized filtered seawater, first at a density of about 100 embryos per ml and in 3 l glass jars oxygenated by a motorized paddle. At 48 h postfertilization, the culture concentration was adjusted to about one larva per ml and from then about 95% of the seawater was renewed every 2 or 3 days. Following water renewal, the larvae were fed ad libidum with freshly grown *Rhodomonas lens* microalgae. Brachiolaria larvae started to settle on the glass jars and to undergo metamorphosis between 1 and 2 months postfertilization. After metamorphosis, juveniles were collected from the glass jars by being first relaxed in a 1:1 mix of 7.5% $MgCl_2$ and filtered seawater and then gently detached using a paintbrush.

X-ray microcomputed tomography

For X-ray micro-CT analyses, *P. miniata* young juveniles of the same size as those used for RNA tomography were relaxed in a 1:1 mix of 7.5% $MgCl_2$ and filtered seawater for 10 min and then fixed in a modified PHEM buffer[60] (90 mM PIPES, 37 mM HEPES, 14 mM EGTA, 30 mM $MgCl_2$, 9% fructose) overnight at 4 °C. The samples were then washed in modified PHEM buffer, before being counterstained in 2% osmium tetroxide in deionized water for 2 h. Following staining, the samples were washed extensively in deionized water, gradually dehydrated in ethanol and stored in ethanol at 4 °C. Before imaging, samples were dried and then pinned on their aboral side to an imaging support. Scanning was carried out using a Zeiss Xradia 520 Versa 3D X-ray microscope. Specimens were scanned at a resolution of 12.138 µm per voxel. To identify different tissues in the scans, regions of interest were segmented using Dragonfly v.2022.2. For segmentation, the deep learning tool was used to train a 3D U-net model, which has been shown to be ideal for rapid and accurate automatic biomedical image segmentation[61]. The U-net model had nine classes, corresponding to different tissue types and was trained for 75 epochs (15.5 h) using a training set of 15 manually segmented slices from the dataset. During model training, a data augmentation factor of 2 was used, including horizontally and vertically slipping the data, rotation, shearing and zoom. Following model training, this U-net was used to automatically segment and identify our nine different tissue classes. Following the initial deep learning-based segmentation, the nine classes were reduced to the five regions of interest shown in the 3D model (endoskeleton, digestive tract, musculature, water vascular system and central nervous system) via the merging of classes relating to similar tissue types (for instance, combining classes pertaining to different types of endoskeletal tissue). At this point, further segmentation was carried out manually in Dragonfly to clean up regions of interest and to produce 3D models and mesh files for visualization. After segmentation, the consistency between the size of the anatomical features reconstructed from the micro-CT scans and the extent of tissue marker expression profiles from the RNA tomography was checked manually. The samples used for micro-CT were registered at the Natural History Museum (London, United Kingdom) under registration no. NHMUK 2023.263. The segmented scans and reconstructed mesh files were deposited on Morphosource under project no. 000529415.

Genomic DNA isolation

The gDNA for genome sequencing was isolated from a dissected arm of the young *P. miniata* specimen 1. Using an extended handle conical tip pestle (Bel-Art Proculture), the arm was homogenized in the presence of the extraction buffer and of proteinase K. The gDNA was then isolated using the DNeasy Blood and Tissue Kit (Qiagen) following the manufacturer's instructions.

Genome sequencing

Ultra-low input HiFi library preparation. Using gDNA from the arm of specimen 1, we generated a HiFi genome of *P. miniata*. The general workflow is described in Supplementary Fig. 2e. As the gDNA isolated from the arm was predominantly shorter than the 10–15 kb which is recommended size for HiFi genomic library creation, size selection was performed before doing an ultra-low input (ULI) amplification and library preparation to remove fragments less than 7 kb. The size selection was done on a SAGE BluePippin system using the 0.75% agarose dye-free gel cassette and the S1 marker (SAGE). Approximately 100 ng of DNA was recovered after size selection and used as input for the ULI PCR-based HiFi library protocol. The sample was amplified using the SMRTbell gDNA Amplification Kit (PacBio) and a HiFi SMRTbell library was constructed using the SMRTbell Express Template Prep Kit 2.0 (PacBio) following manufacturer's recommended protocol. After library construction, a final size selection was performed on the SAGE BluePippin as previously described using a size cutoff of 7 kb. Library size was characterized on an Agilent 2100 BioAnalyzer using the DNA 12000 kit (Agilent). The extra size selection ensured having a final library with a fragment size range greater than 7 kb.

HiFi reads sequencing. Sequencing reactions were performed on the PacBio Sequel II System with the Sequel Sequencing Kit 2.0 (PacBio). The kit uses a circular consensus sequencing (CCS) mode which provides more than 99.5% single-molecule read accuracy[62]. The samples were pre-extended without exposure to illumination for 2 h to enable the polymerase enzymes to transition into the highly progressive strand-displacing state and sequencing data were collected for 30 h to ensure maximal yield of high-quality CCS reads. CCS reads were generated from the data using the SMRT Link v.9.0 (PacBio). For the genomic HiFi sequencing, the library was bound to the sequencing enzyme using the Sequel II Binding Kit 2.2 and the Internal Control Kit 1.0 (PacBio). The HiFi reads generated 15,614,751 HiFi reads with a mean read length of 9,039 ± 1,671 base pairs (bp) (Supplementary Fig. 3e).

Genome assembly. Before de novo genome assembly, the reads were trimmed on the ends to remove any PCR primer sequences from the ultra-low amplification process using lima v.2.2 (PacBio). The forward sequence of the amplification adaptor used was AAGCAGTGGTAT CAACGCAGAGTACT. Once the HiFi reads were trimmed, a filtering step was performed to remove duplicate reads from the PCR step using SMRT link v.9.0. After removing duplicate reads, the HiFi reads (approximately 100× genomic coverage) were used to generate a draft diploid assembly using Hifiasm v.0.15 (ref. 63). This resulted in two highly contiguous haplotype primary assemblies of 680 and 674 Mb, respectively (Supplementary Table 5). Assembly completeness was assessed with the benchmarking single-copy orthologue[64] (BUSCO v.3.0) gene set for Metazoa at 94.8% for each of the individual haplotype

primary assemblies and 96.2% overall for the diploid assembly as a whole (Supplementary Fig. 3d and Supplementary Table 4). The two haplotypes were deposited at DDBJ/ENA/GenBank under accession numbers JAPJSQ000000000 and JAPJSR000000000.

RNA tomography section preparation and RNA extraction

The three arms embedded in HistoPrep medium were cryosectioned using a Leica CM3050-S microtome along the appropriate dimensions: proximodistal (P–D), oral–aboral (O–A) or mediolateral (M–L) (Supplementary Fig. 2a–c). The blocks used for the P–D and O–A dimensions came from specimen 1, whereas the block used for the M–L dimension came from specimen 2. Slice thickness was set to 25 µm for the P–D and O–A dimensions and to 30 µm for the M–L dimension, resulting in total in 430, 160 and 160 slices for the three respective dimensions. Every 20 (P–D and O–A) or 10 (M–L) contiguous slices were pooled together into 1.5 ml tubes during the sectioning of the blocks. These resulted in a total of 22 tubes for the P–D dimension, 8 tubes for the O–A dimension and 16 tubes for the M–L dimension (Supplementary Fig. 2d). Each tube was then processed for RNA extraction using a modified Trizol/RNeasy RNA extraction protocol[65]. In each tube, the slices were homogenized in 1 ml of Trizol using an extended handle conical tip pestle (Bel-Art Proculture). After vigorously mixing the Trizol homogenate with chloroform, each tube was centrifuged at 10,000*g* for 18 min at 4 °C. The aqueous phase containing the RNA was carefully removed and the RNA was further purified using the RNeasy Plus Micro Kit (Qiagen) following the manufacturer's instructions.

RNA tomography

Barcoded cDNA IsoSeq SMRTbell library preparation. Using RNA isolated from the three sets of cryosections, we generated a RNA tomography[28,66] dataset for *P. miniata* juveniles. The general workflow is described in Supplementary Fig. 2e. Barcoded PacBio IsoSeq SMRTbell libraries were constructed using the SMRTbell Express Template Prep Kit 2.0 (PacBio) following the manufacturer's instructions. We used a set of 22 barcoded sequences (Supplementary Table 1) which were combined with each RNA extract (Supplementary Table 2). Typically, 12–14 PCR amplification cycles were used to generate enough barcoded double-stranded complementary DNA (cDNA) for the library preparation and subsequent sequencing runs (Supplementary Table 2).

Library sequencing. For the Iso-seq transcript libraries, library was bound to the sequencing enzyme using the Sequel II Binding Kit 2.1 and Internal Control Kit 1.0 (PacBio) and the sequencing reactions were performed on the PacBio Sequel II System. The three dimensions were sequenced independently because there were shared barcodes between the different libraries. We obtained a total of 71,582,642 reads (Supplementary Table 3) with a mean read length of 3,843, 3,152 and 2,450 bp for the P–D, O–A and M–L dimensions, respectively (Supplementary Fig. 3a). In addition, HiFi read length distributions were consistent across each barcode within the respective RNA tomography dimension (Supplementary Fig. 3b). Sequence read archives were deposited at DDBJ/ENA/GenBank under Bioproject PRJNA873766 and individual accession numbers for each barcode are provided in Supplementary Table 3. Recent advancements in full-length transcript concatenation protocols[67], as well as higher multiplexed SMRT sequencing flow cells have increased throughput with a concomitant decrease in sequencing cost over a single 24 h run. Genomic, epigenetic and transcript datasets can now all originate from the same individual greatly improving the mappability and subsequent analysis of transcripts in highly polymorphic non-model organisms in which gene sequences can differ by more than 5% in coding regions and as much as 40% in untranslated region (UTR) sequences which complicate short read transcript alignment and reliable quantitation.

Iso-seq reads demultiplexing and refining. For each HiFi read file generated, the data were demultiplexed into barcode-specific read files using lima v.2.2 (PacBio) and the barcodes listed in Supplementary Table 1. Once the data were demultiplexed each read file was refined to include only full-length non-chimaeric reads using isoseq3 v.3.4.0 (ref. 68). Chimaeras were identified by inclusion of 5′ or 3′ real-time PCR primer sequences internal to the initial 'full-length' HiFi read. The primer sequences used were NEB_5P (GCAATGAAGTCGCAGGGTTGGG), Clontech_5P (AAGCAGTGGTATCAACGCAGAGTACATGGGG) and NEB_Clontech_3P (GTACTCTGCGTTGATACCACTGCTT). Transcript clusters were identified using Cupcake v.25.2.0 (ref. 69) which leverages a genomic reference alignment-based strategy to identify redundant isoforms/transcripts for gene loci. We leveraged the diploid assembly to minimize dropouts that might be caused by haplotype-specific null alleles and/or poor mapping between haplotypes for the same locus. Comparative alignment of the two haplotype-derived transcriptomes facilitated further collapse of the gene set to one representative per loci.

Transcriptome generation and curation. Using each haplotype primary assembly, the complete set of full-length non-chimaeric transcript reads (FLNC) were clustered and collapsed to reduce gene redundancy while maintaining the highest possible level of gene completeness. The complete set of FLNC reads across all three combined RNA tomography datasets were clustered from a list of input bam files based on each of the haplotype-specific primary assemblies. Minimap2 v.2.21 (ref. 70) was used to align the FLNC reads to each primary assembly and Sqanti2 v.7.4 (ref. 71) was used to cluster and filter redundancies. Once minimal transcript sets were obtained for each haplotype, a comparative alignment between the sets was performed using Minimap2 v.2.21 aligner to find unique transcripts between the two. From the ouput paf files, transcripts unique to haplotype 2 which were not present in the haplotpye 1 were identified, filtered out from the haplotype 2 set and added to the haplotype 1 set to obtain a more complete single-copy transcript set.

Manually curated developmental genes of interest were identified (see below). All sequences in our 'single-copy' transcript set were aligned using TBLASTX to the manually curated set to (1) remove any duplication of these key transcripts in our reference transcriptome (for example, the high polymorphism rate resulted in both copies of some of the manually curated genes being present) and (2) remove partial duplications (non-full-length transcripts matching the manually curated set). The result of this curation step was to ensure that for every gene of interest, we had only one sequence in our reference transcriptome to maintain accurate downstream quantification. Given the occasional duplication of transcripts in our reference transcriptome (eliminated for our genes of interest), it is assumed that the uncurated transcripts have some level of duplication.

Once we derived a near-complete curated transcriptome for *P. miniata*, the barcode-specific demultiplexed RNA tomography datasets were aligned to the transcriptome reference using Minimap2 v.2.21. The final refined *P. miniata* transcriptome comprised 25,794 transcripts and represented a nearly complete (91.5%) set of metazoan BUSCO genes (Supplementary Fig. 3d and Supplementary Table 4). Transcript expression counts for each of the 25,794 gene models in our reference transcriptome were tallied using a simple Perl v.5.30.1 script that only counted primary alignments (no supplementary alignments) with a quality value of 15 or greater. Each section was tallied independently and the data merged. The alignment counts for each section were normalized to the total reads for each barcode to allow spatial comparisons to be made across each dimension of the RNA tomography dataset. This was done to account for variable recovery of total RNA in each barcoded section (Supplementary Fig. 3c).

Orthologues identification

P. miniata orthologues of developmental genes of interest, which included 36 A–P patterning-related genes, 6 D–V specification and

patterning-related genes, 3 limb P–D patterning-related genes, the pan-neuronal marker *elav*, the gut marker *lox* and the hydrocoel marker *patched* were identified from the FLNC reads by reciprocal best blast hit and validated by phylogenetic trees (Supplementary Fig. 4). Nucleotide sequences for these transcripts were deposited at DDBJ/ENA/GenBank and accession numbers are provided in Supplementary Table 6. Trees were calculated with both the maximum likelihood and Bayesian inference methods. Maximum likelihood trees were calculated in MEGA v.7.0.26 (ref. 72) with the robustness of each node being estimated by bootstrap analyses (in 1,000 pseudoreplicates). Bayesian inference trees were calculated using MrBayes v.3.1.2 (ref. 73) in 1,000,000 generations with sampling of trees every 100 generations and a burn-in period of 25%. The branching pattern of the maximum likelihood tree was retained in the final tree figure, except for TALE class homeobox transcription factors for which the bayesian topology was retained, and displaying in both cases at each node the bootstrap support of the maximum likelihood analysis as well as the posterior probability support of the bayesian inference analysis.

RNA tomography analyses

RNA tomography analyses were performed in R v.4.1.2 using custom-written code. For downstream analyses, the 22 sections of the P–D dimension were merged pairwise by simple addition of the read counts mapping for each transcripts, bringing the final number of sections in the P–D dimension to 11 (Supplementary Fig. 2d). In addition, section 14 of the M–L dataset was removed because it yielded a total read count 77% lower than the average total read count per section for the M–L dimension, which could have biased the quantification analyses. To maintain the symmetry in the M–L dimension, section 3 was also removed, bringing the final number of sections in the M–L dimension to 14 (Supplementary Fig. 2d).

Individual read counts from each section of the three RNA tomography dimensions were normalized against the total read count of the section to account for sequencing depth differences between the three dimensions and for geometrical disparities between the different sections of a single dimension. Because we were interested in the profile of highly expressed and variable genes, whereas genes with a uniform expression across the sections were poorly informative, a cutoff was applied to discard genes which consistently had the 20% lowest average expression level or 20% lowest variability in all of the three dimensions, resulting in a final set of 21,847 gene models (Supplementary Fig. 3f). Of the 36 A–P patterning-related genes investigated in this study, four of them fell below the cutoff and were excluded from the computational analyses because of their low expression levels: *rx*, *dlx*, *hox11/13a* and *hox11/13c* (Supplementary Fig. 3f). For further analyses, the expression levels of each gene along each of the three dimension sections was transformed into *z*-score.

For the clustering analysis, the dimensionality of the dataset was first reduced using a PCA performed simultaneously on the three dimensions of the RNA tomography. Kaiser–Guttman's criterion[74] was used to select the significant PCs of the PCA. Then, the coordinates of the transcripts along the retained PCA axes were used to compute the Euclidean distance matrix and hierarchical agglomerative clustering using Ward's aggregation to produce an expression profile dendrogram[75]. Following the methodology established in previous RNA tomography studies[28], we estimated a maximal number of 12 clusters based on discernible anatomical features in the Spearman correlation matrices of the sections (Extended Data Fig. 1f). However, the relevant number of clusters was probably lower than 12 because of the lack of independence of gene expression between the three dimensions. We thus used a silhouette index[76] to evaluate the consistency of clusters when choosing between 2 and 12 clusters. The silhouette index indicated that 7 was the most appropriate number of clusters and this number also minimized redundancy between the different gene expression profiles.

For the hypothesis testing, we determined the ranking of the 36 investigated A–P patterning-related genes on the basis of their expression profiles in the hemichordate *S. kowaleskii*, which is the closest bilateral echinoderm-relative with an extensive dataset of A–P patterning gene expression profiles[4,5,37,48,77–80]. Gene expression patterns in other hemichordate studies are largely consistent with those observed in *S. kowalevskii*[35,81]. The 36 genes were divided into seven groups on the basis of their expression domains (anterior proboscis (A), proboscis (B), anterior collar (C), posterior proboscis and collar (D), collar–trunk boundary (E), trunk (F) and posterior tip of the trunk (G)) (Supplementary Fig. 6). Within each group, genes were ranked on the basis of their expression pattern and, when required, tied on the basis of the available gene expression patterns in other closely related species. We were confident that the assignment of each gene to the groups A to G on the basis of their expression profile in *S. kowalevskii* was robust to interpretation biases. On the other hand, given that the genes expressed in these groups are more or less coincident in parts of the A–P axis of *S. kowalevskii*, we recognized that the internal gene ranking within each group was more subject to possible interpretation biases.

To test the Spearman correlation between the A–P patterning-related gene ranking and the gene expression profiles along the three dimensions of the RNA tomography, the symmetrical sections of the M–L were averaged pairwise (1 and 14, 2 and 13 and so on). We then used the highest *z*-score as a readout for the position of each gene in each dimension and correlated it to the ranking of the A–P genes as described above. The significance of this raw correlation was assessed by a two-sided Spearman correlation test. In addition, each of the seven groups of genes was independently removed to assess its contribution to the correlation. However, this approach is subjected to two potential sources of errors, resulting (1) from choosing the single highest *z*-score value for the position of genes with multimodal expression profiles and (2) from biases in determining the ranking of the A–P genes within each of the seven gene groups, as mentioned above. To account for these biases, we also ran 10^6 independent correlations, with each correlation (1) probabilistically determining the position of each gene by using the *z*-score as a law of probability and (2) randomly shuffling the ranking of the genes within the seven gene groups. The distribution of the 10^6 correlations values was then compared across the three dimensions of the RNA tomography using a two-sided Wilcoxon rank test.

In situ hybridization

Short in situ hybridization antisense DNA probes were designed on the basis of the split-probe design of HCR v.3.0 (ref. 82) using HCR 3.0 Probe Maker[83] with adjacent B1, B2 or B3 amplification sequences, depending on the genes (Supplementary Table 7). Between 14 and 33 probe pairs were designed for each gene including the coding sequence and for some of them adjacent 5′ and 3′ UTRs. The probe pairs were then ordered as oligo pools (Integrated DNA Technology) and suspended in nuclease-free water at a concentration of 0.5 µM.

For in situ hybridization, *P. miniata* brachiolaria larvae, metamorphosing larvae and juveniles were incubated in fixation buffer (1× phosphate buffered saline (PBS), 0.1 M MOPS, 0.5 M NaCl, 2 mM EGTA, 1 mM $MgCl_2$) containing 3.7% formaldehyde overnight at 4 °C. Fixed samples were then dehydrated in methanol and stored at −20 °C for at least 24 h and up to several months. The samples were progressively rehydrated in PBS containing 0.1% Tween-20 (PBST). They were permeabilized in detergent solution (1.0% SDS, 0.5% Tween-20, 150 mM NaCl, 1 mM EDTA (pH 8), 50 mM Tris-HCl at pH 7.5) 30 min for larvae and 2 h for juveniles. For juveniles, this step was followed by an extra permeabilization step in 4 µg ml^{-1} proteinase K (Sigma-Aldrich) for 10 min at 37° and postfixation in 3.7% formaldehyde for 25 min. The samples were extensively washed in PBST and then in 5× saline sodium citrate buffer containing 0.1% Tween-20 (SSCT), before being prehybridized in hybridization buffer (Molecular Instruments) for 1 h at 37 °C. The probes were then added to the hybridization buffer at a final concentration of 0.05 µM

and the samples were allowed to hybridize at 37 °C overnight under gentle agitation. Following hybridization, the samples were washed four times for 30 min in probe wash buffer (Molecular instruments) at 37 °C and then in 5× SSCT at room temperature. They were then pre-amplified in amplification buffer (Molecular Instruments) for 30 min. Meanwhile, H1 and H2 components of the HCR hairpins B1, B2 or B3 coupled to either Alexa546 or Alexa647 fluorophores (Molecular Instruments) were incubated separately at 95 °C for 90 s, cooled down to room temperature in the dark and then pooled together before being added to the amplification buffer at a final concentration of 60 nM. The amplification was then performed overnight at room temperature. The samples were subsequently washed four times for 30 min in 5× SSCT and incubated in PBST containing 1:1,000 DAPI (Invitrogen) for 3 h. Finally, the samples were cleared in a series of 20%, 40%, 60% and 80% fructose diluted in PBS. Each fructose bath was carried out for at least 1 h. Cleared samples were mounted in 80% fructose diluted in PBS for imaging, which was done using a Zeiss LSM700 confocal microscope. For each sample, series of optical sections were taken with a *z*-step interval of 2–3 µm. Multichannel acquisitions were obtained by sequential imaging. Confocal optical sections spanning regions of interest along the O–A axis were compiled into maximum intensity *z*-projections using ImageJ v.1.52g (ref. 84) and assembled into figure using Adobe Illustrator v.15.0.0.

The specificity of the antisense DNA probes and amplification hairpins was validated by running the protocol without hairpins and probes or with hairpins alone and comparing antisense and sense probe sets for *nkx2.1* (Supplementary Fig. 7). The consistency of the expression patterns obtained through this method was further validated by comparisons of *elav*, *nkx2.1*, *dmbx* and *otx* with colorimetric whole-mount in situ hybridization using single antisense RNA probes as described previously[85] (Supplementary Fig. 7). To ensure reproducibility of the in situ hybridization expression patterns, each gene was surveyed in at least two independent experiments and for each experiment at least ten samples were analysed and gave consistent results.

Immunohistochemistry

Immunofluorescence stainings were performed as described previously[86] using an anti-acetylated tubulin produced in mouse (Sigma-Aldrich, reference no. T7451-100UL, lot no. 036M4856V) diluted at 1:200. Secondary antibody used was a goat anti-mouse IgG (H + L) coupled to Alexa Fluor 647 (Invitrogen, reference no. A21235, lot no. 2270554) diluted at 1:500. For endoskeleton stainings, larvae reaching the brachiolaria stage were incubated in seawater supplemented with 5 ml per 1 l of saturated calcein solution (Sigma-Aldrich), a fluorescent calcium analogue which is incorporated into the endoskeleton[87], until the completion of the metamorphosis. The postmetamorphic juveniles were then fixed, counterstained with DAPI and cleared following the same procedure as for immunofluorescence stainings. Imaging was done following the same procedure as for in situ hybridizations.

Reporting summary

Further information on research design is available in the Nature Portfolio Reporting Summary linked to this article.

Data availability

Specimens used for micro-CT analyses are registered at the Natural History Museum (London, UK) under registration no. NHMUK 2023.263. The segmented scans and reconstructed mesh files are available in Morphosource under project no. 000529415. Genome haplotypes are available at DDBJ/ENA/GenBank under accession nos. JAPJSQ000000000 and JAPJSR000000000. Sequence read archives for RNA sequencing are available at DDBJ/ENA/GenBank under Bioproject PRJNA873766. RNA tomography dataset is available at Zenodo: https://doi.org/10.5281/zenodo.8327479. Source data are provided with this paper.

Code availability

Custom code used for RNA tomography analyses is available at Zenodo: https://doi.org/10.5281/zenodo.8327479.

60. Montanaro, J., Gruber, D. & Leisch, N. Improved ultrastructure of marine invertebrates using non-toxic buffers. *PeerJ* **4**, e1860 (2016).
61. Ronneberger, O., Fischer, P. & Brox, T. in *Medical Image Computing and Computer-Assisted Intervention—MICCAI 2015* (eds Navab, N. et al.) 234–241 (Springer, 2015).
62. Wenger, A. M. et al. Accurate circular consensus long-read sequencing improves variant detection and assembly of a human genome. *Nat. Biotechnol.* **37**, 1155–1162 (2019).
63. Cheng, H., Concepcion, G. T., Feng, X., Zhang, H. & Li, H. Haplotype-resolved de novo assembly using phased assembly graphs with hifiasm. *Nat. Methods* **18**, 170–175 (2021).
64. Simão, F. A., Waterhouse, R. M., Ioannidis, P., Kriventseva, E. V. & Zdobnov, E. M. BUSCO: assessing genome assembly and annotation completeness with single-copy orthologs. *Bioinformatics* **31**, 3210–3212 (2015).
65. Bellantuono, A. J., Granados-Cifuentes, C., Miller, D. J., Hoegh-Guldberg, O. & Rodriguez-Lanetty, M. Coral thermal tolerance: tuning gene expression to resist thermal stress. *PLoS ONE* **7**, e50685 (2012).
66. Kruse, F., Junker, J. P., Van Oudenaarden, A. & Bakkers, J. Tomo-seq: a method to obtain genome-wide expression data with spatial resolution. *Methods Cell. Biol.* **135**, 299–307 (2016).
67. Al'Khafaji, A. M. et al. High-throughput RNA isoform sequencing using programmable cDNA concatenation. *Nat. Biotechnol.* https://doi.org/10.1038/s41587-023-01815-7 (2023).
68. Mattick, J. IsoSeq v.4.00. GitHub https://github.com/PacificBiosciences/IsoSeq (2023).
69. Tseng, E. cDNA cupcake v.25.2.0. GitHub https://github.com/Magdoll/cDNA_Cupcake/wiki (2022).
70. Li, H. Minimap2: pairwise alignment for nucleotide sequences. *Bioinformatics* **34**, 3094–3100 (2018).
71. Tardaguila, M. et al. SQANTI: extensive characterization of long-read transcript sequences for quality control in full-length transcriptome identification and quantification. *Genome Res.* **28**, 396–411 (2018).
72. Kumar, S., Stecher, G. & Tamura, K. MEGA7: Molecular Evolutionary Genetics Analysis version 7.0 for bigger datasets. *Mol. Biol. Evol.* **33**, 1870–1874 (2016).
73. Huelsenbeck, J. P. & Ronquist, F. MRBAYES: Bayesian inference of phylogenetic trees. *Bioinformatics* **17**, 754–755 (2001).
74. Guttman, L. Some necessary conditions for common-factor analysis. *Psychometrika* **19**, 149–161 (1954).
75. Murtagh, F. & Legendre, P. Ward's hierarchical agglomerative clustering method: which algorithms implement Ward's criterion? *J. Classif.* **31**, 274–295 (2014).
76. Rousseeuw, P. J. Silhouettes: a graphical aid to the interpretation and validation of cluster analysis. *J. Comput. Appl. Math.* **20**, 53–65 (1987).
77. Aronowicz, J. & Lowe, C. J. Hox gene expression in the hemichordate *Saccoglossus kowalevskii* and the evolution of deuterostome nervous systems. *Int. Comp. Biol.* **46**, 890–901 (2006).
78. Lemons, D., Fritzenwanker, J. H., Gerhart, J., Lowe, C. J. & McGinnis, W. Co-option of an anteroposterior head axis patterning system for proximodistal patterning of appendages in early bilaterian evolution. *Dev. Biol.* **344**, 358–362 (2010).
79. Satoh, N. et al. On a possible evolutionary link of the stomochord of hemichordates to pharyngeal organs of chordates. *Genesis* **52**, 925–934 (2014).
80. Fritzenwanker, J. H., Uhlinger, K. R., Gerhart, J., Silva, E. & Lowe, C. J. Untangling posterior growth and segmentation by analyzing mechanisms of axis elongation in hemichordates. *Proc. Natl Acad. Sci. USA* **116**, 8403–8408 (2019).
81. Kaul-Strehlow, S., Urata, M., Praher, D. & Wanninger, A. Neuronal patterning of the tubular collar cord is highly conserved among enteropneusts but dissimilar to the chordate neural tube. *Sci. Rep.* **7**, 7003 (2017).
82. Choi, H. M. et al. Third-generation in situ hybridization chain reaction: multiplexed, quantitative, sensitive, versatile, robust. *Development* **145**, dev165753 (2018).
83. Kuehn, E. et al. Segment number threshold determines juvenile onset of germline cluster expansion in *Platynereis dumerilii*. *J. Exp. Zool. B* **338**, 225–240 (2022).
84. Schneider, C. A., Rasband, W. S. & Eliceiri, K. W. NIH Image to ImageJ: 25 years of image analysis. *Nat. Methods* **9**, 671–675 (2012).
85. Lowe, C. J., Tagawa, K., Humphreys, T., Kirschner, M. & Gerhart, J. Hemichordate embryos: procurement, culture and basic methods. *Methods Cell. Biol.* **74**, 171–194 (2004).
86. Formery, L. et al. Neural anatomy of echinoid early juveniles and comparison of nervous system organization in echinoderms. *J. Comp. Neurol.* **529**, 1135–1156 (2021).
87. Thompson, J. R., Paganos, P., Benvenuto, G., Arnone, M. I. & Oliveri, P. Post-metamorphic skeletal growth in the sea urchin *Paracentrotus lividus* and implications for body plan evolution. *EvoDevo* **12**, 3 (2021).

Acknowledgements We would like to thank F. Benedetti and R. Elahi for helping with RNA tomography analyses; A. Vailionis, P. Vyas and the Stanford Nano Shared Facility for helping with X-ray micro-CT; J. Grossman for the ambulacral-anterior model schematics; A. Formery for providing the 3D models of the RNA tomography sections; A. Rutledge for helping with animal husbandry; and V. Hinman for providing clones for preliminary analyses. We also thank G. A. Wray, T. Lacalli, R. Mooi, J. C. Croce and members of the Rokhsar and Lowe laboratories for discussions. This work was supported by a Leverhulme Trust Early Career Fellowship to J.R.T.,

a NASA grant to C.J.L. (NNX13AI68G), an NSF grant to C.J.L. (1656628) and Chan Zuckerberg BioHub funding to D.S.R. and C.J.L. For the purpose of open access, the author has applied a CC BY public copyright license to any Author Accepted Manuscript version arising from this submission.

Author contributions Experiments were designed by L.F., P.P., D.R.R. and C.J.L. Preliminary data were acquired by I.K., J.M. and K.R.U. Genome sequencing was done by P.P. and D.R.R. RNA tomography sectioning and sequencing were done by P.P., M.P., D.R.R. and C.J.L. RNA tomography analyses were performed by L.F. and D.S.R. Micro-CT preparation was done by L.F. and segmentation of the scans was done by J.R.T. Immunofluorescence, HCRs and imaging were performed by L.F. Data were analysed by L.F., D.S.R. and C.J.L. The manuscript was written by L.F., D.S.R. and C.J.L. with input from all authors.

Competing interests P.P. and D.R.R. are employees and shareholders of Pacific Biosciences. The remaining authors declare no competing interests.

Additional information

Supplementary information The online version contains supplementary material available at https://doi.org/10.1038/s41586-023-06669-2.

Correspondence and requests for materials should be addressed to L. Formery or C. J. Lowe.

Peer review information *Nature* thanks Andreas Hejnol and the other, anonymous, reviewer(s) for their contribution to the peer review of this work. Peer reviewer reports are available.

Reprints and permissions information is available at http://www.nature.com/reprints.

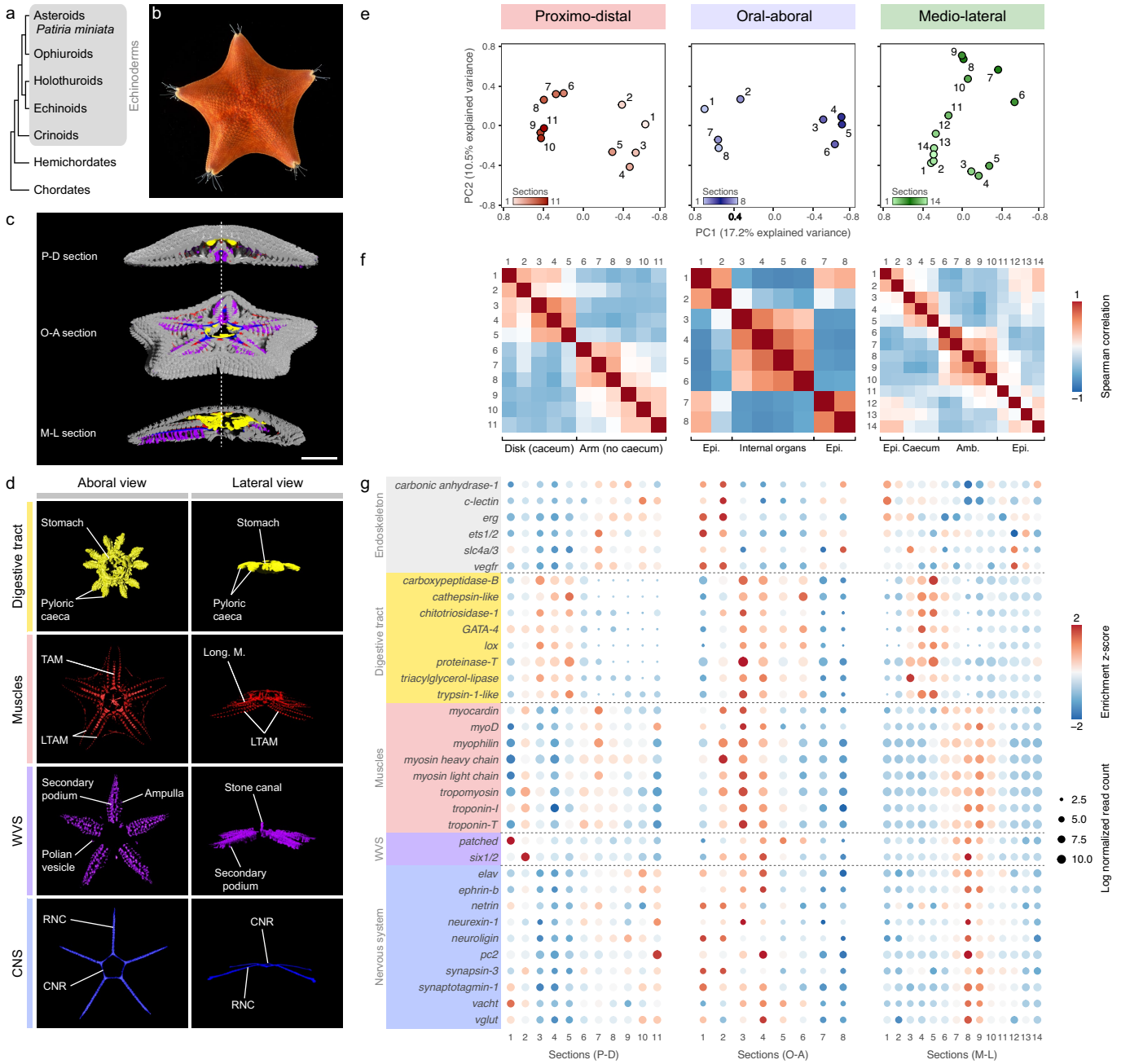

Extended Data Fig. 1 | *Patiria miniata* anatomy is reflected by RNA tomography. a, Phylogenetic position of *P. miniata* within deuterostomes, the grey box highlights the echinoderm phylum. **b**, Young adult *P. miniata*, viewed from the aboral side. **c**,**d**, Reconstructions of a young juvenile *P. miniata* scanned by micro-CT and segmented to highlight the main anatomical features of the animal, including the endoskeleton (grey), the digestive tract (yellow), the main body muscles (red), the water vascular system (WVS; purple) and the central nervous system (CNS; blue). **c**, Lateral views showing virtual sections of the micro-CT reconstruction along the proximodistal (P–D), oral–aboral (O–A) and mediolateral (M–L) dimensions used in the RNA tomography. Scale bar, 1 mm. **d**, Details of the different anatomical features shown in aboral or lateral views. The different panels are shown at the same scale. TAM: transverse ambulacral muscle; LTAM: lateral transverse ambulacral muscle; Long. M: longitudinal muscle; RNC: radial nerve cord; CNR: circumoral nerve ring. **e**, Principal component analysis of the RNA tomography sections. For each dimension the sections are colour-coded according to the geometry of the animal. **f**, Spearman correlations between the sections of the RNA tomography in each of the three dimensions. Epi: epidermis; Amb: ambulacrum. **g**, Expression profiles along the three dimensions of the RNA tomography for tissue marker genes known based on published literature to be expressed in the endoskeleton (grey), digestive tract (yellow), muscles (red), WVS (purple) and in the nervous system (blue) are consistent with the anatomy of the animal. Note that in the case of digestive tract markers, there is a left shift of expression in the M–L dimension that we assume resulted from displacement of the pyloric caeca during the dissection of the arm.

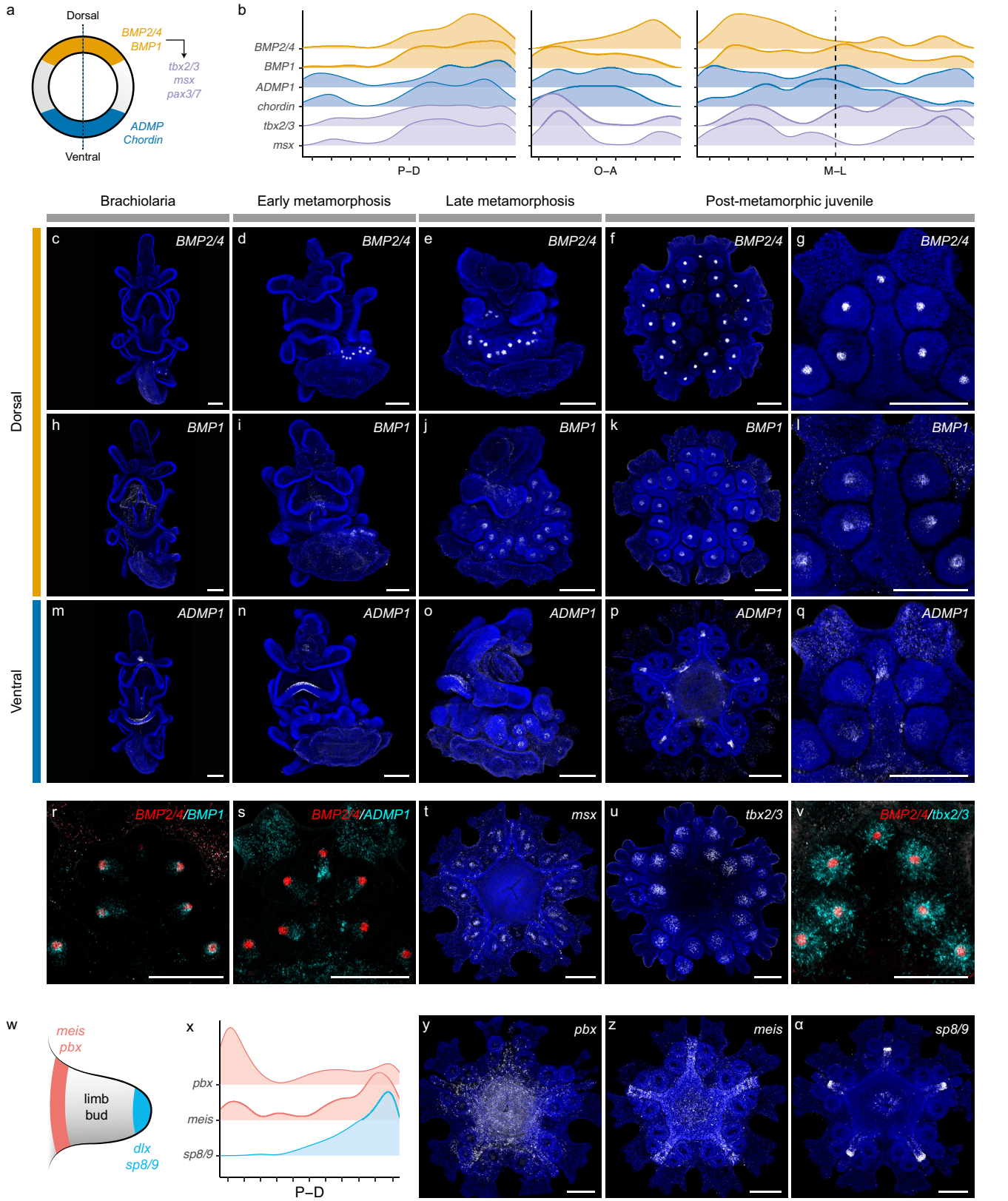

Extended Data Fig. 2 | Dorsoventral and appendage patterning in *Patiria miniate*. **a**, Schematic representation of D–V patterning in bilaterians. **b**, Expression profile of D–V specification and patterning genes along the P–D, O–A and M–L dimensions of the RNA tomography. For the M–L dimension, the dotted line indicates the midline. **c**-**v**,**y**-**α**, HCRs of *P. miniata* brachiolariae (**c**,**h**,**m**), early metamorphosis (**d**,**i**,**n**), late metamorphosis (**e**,**j**,**o**) and postmetamorphic juveniles (**f**,**g**,**k**,**l**,**p**-**v**,**y**-**α**) imaged from the oral side. In **c**-**q**,**t**,**u**,**y**-**α**, specimens are counterstained with DAPI (blue). **g**,**l**,**q**,**r**,**s**,**v**, Magnification of a single ambulacrum. **c**-**v**, Expression patterns of genes involved in D–V axis specification and patterning. **w**, Schematic representation of limb proximodistal patterning in bilaterians. **x**, Expression profile of limb proximodistal patterning genes along the P–D dimension of the RNA tomography. **y**-**α**, Expression patterns of genes involved in limb proximodistal patterning. Scale bars, 100 µm.

nature portfolio

Corresponding author(s): Laurent Formery, Christopher J. Lowe

Last updated by author(s): Jul 24, 2023

Reporting Summary

Nature Portfolio wishes to improve the reproducibility of the work that we publish. This form provides structure for consistency and transparency in reporting. For further information on Nature Portfolio policies, see our Editorial Policies and the Editorial Policy Checklist.

Statistics

For all statistical analyses, confirm that the following items are present in the figure legend, table legend, main text, or Methods section.

n/a	Confirmed	
☐	☒	The exact sample size (*n*) for each experimental group/condition, given as a discrete number and unit of measurement
☐	☒	A statement on whether measurements were taken from distinct samples or whether the same sample was measured repeatedly
☐	☒	The statistical test(s) used AND whether they are one- or two-sided *Only common tests should be described solely by name; describe more complex techniques in the Methods section.*
☐	☒	A description of all covariates tested
☐	☒	A description of any assumptions or corrections, such as tests of normality and adjustment for multiple comparisons
☐	☒	A full description of the statistical parameters including central tendency (e.g. means) or other basic estimates (e.g. regression coefficient) AND variation (e.g. standard deviation) or associated estimates of uncertainty (e.g. confidence intervals)
☐	☒	For null hypothesis testing, the test statistic (e.g. *F*, *t*, *r*) with confidence intervals, effect sizes, degrees of freedom and *P* value noted *Give P values as exact values whenever suitable.*
☐	☒	For Bayesian analysis, information on the choice of priors and Markov chain Monte Carlo settings
☒	☐	For hierarchical and complex designs, identification of the appropriate level for tests and full reporting of outcomes
☒	☐	Estimates of effect sizes (e.g. Cohen's *d*, Pearson's *r*), indicating how they were calculated

Our web collection on statistics for biologists contains articles on many of the points above.

Software and code

Policy information about availability of computer code

Data collection	SMRT Link v.9.0
Data analysis	Lima v2.2; Hifiasm v.0.15; BUSCO v.3.0; Isoseq3 v.3.4.0; Cupcake v.25.2.0; Minimap2 v.2.21; Sqanti2 v.7.4; MEGA v.7.0.26; MrBayes v.3.1.2; R v.4.1.2; Perl v.5.30.1; HCR 3.0 Probe Maker v.1.0; ImageJ v.1.52g; Adobe Illustrator v.15.0.0; Dragonfly v.2022.2 Custom code used for RNA tomography analyses is available at Zenodo under DOI 10.5281/zenodo.8327479.

For manuscripts utilizing custom algorithms or software that are central to the research but not yet described in published literature, software must be made available to editors and reviewers. We strongly encourage code deposition in a community repository (e.g. GitHub). See the Nature Portfolio guidelines for submitting code & software for further information.

Data

Policy information about availability of data

All manuscripts must include a data availability statement. This statement should provide the following information, where applicable:

- Accession codes, unique identifiers, or web links for publicly available datasets
- A description of any restrictions on data availability
- For clinical datasets or third party data, please ensure that the statement adheres to our policy

All data are available upon request. Specimens used for Micro-CT analyses are registered at the Natural History Museum (London, UK) under the registration

number NHMUK 2023.263. The segmented scans and reconstructed mesh files are available in Morphosource under the project number 000529415. Genome haplotypes have been deposited at DDBJ/ENA/GenBank under the accession numbers JAPJSQ000000000 and JAPJSR000000000. Sequence read archives from the RNA tomography were deposited at DDBJ/ENA/GenBank under the bioproject PRJNA873766. SRA Bio-samples ID of RNA tomography sections are listed in Supplementary Table 3. GenBank Accession numbers of genes of interest are provided in Supplementary Table 6. RNA tomography dataset is available at Zenodo under DOI 10.5281/zenodo.8327479. Sequence of the HCR probes in this study are provided in Supplementary Table 7.

Human research participants

Policy information about studies involving human research participants and Sex and Gender in Research.

Reporting on sex and gender	N/A
Population characteristics	N/A
Recruitment	N/A
Ethics oversight	N/A

Note that full information on the approval of the study protocol must also be provided in the manuscript.

Field-specific reporting

Please select the one below that is the best fit for your research. If you are not sure, read the appropriate sections before making your selection.

☒ Life sciences ☐ Behavioural & social sciences ☐ Ecological, evolutionary & environmental sciences

For a reference copy of the document with all sections, see nature.com/documents/nr-reporting-summary-flat.pdf

Life sciences study design

All studies must disclose on these points even when the disclosure is negative.

Sample size	Two individuals were used for RNA tomography, which is standard for this type of experiment. Genome sequencing was done from one of the specimen used for RNA tomography to facilitate alignment. The number of sections pooled for each dimension of the RNA tomography was estimated based on the amount of total RNA extracted per section. Two individuals were prepared and scanned for micro-CT. For immunostainings and in situ hybridization, between 10 and 50 specimens were used per experiment, which is standard for such experiments. The results between the different samples was always consistent.
Data exclusions	For RNA tomography, 2 sections of the L-R dataset out of 16 were excluded. Section 14 was excluded because it yielded a total read count 77% lower than the average total read count per section for the L-R dimension, which could have biased the quantification analyses. To maintain the symmetry in the L-R dimension, section 3 was also excluded, bringing down the final number of sections included in the analysis of the L-R dimension from 16 to 14. No data were excluded from the gene expression pattern analysis.
Replication	Each dimension of the RNA tomography was only performed once, however general correspondance of individual gene read counts across sections after normalization ensured the reproducibility at the level of individual RNAseq experiments on sections within a single dimension. A total of 22 sections were sequenced for the P-D dimension, 16 for the L-R dimension and 8 for the O-A dimension. Two distinct specimens of the same size were scanned and analyzed by micro-CT independantly and gave consistent results. Other experimental techniques such as HCR in situ hybridizations and immunohistochemistry were performed at least 2 times and each time at least 10 specimens were imaged through their entire thickness using a confocal microscope, in order to validate the consistency of the findings and expression patterns. The results between the different samples was always consistent.
Randomization	The individuals used for RNA tomography, genome sequencing and micro-CT were picked randomly out of a pool of animals of similar size. For juvenile rearing, the adult animal used for spawning were selected randomly, and all the juveniles from a culture were fixed. The specimens used for HCR in situ hybridizations or immunohistochemistry and imaging among the pool of fixed juveniles were selected randomly for each experiment.
Blinding	Investigators were not blinded to allocation during experiments and outcome assessment, which is standard for this type of study.

Reporting for specific materials, systems and methods

We require information from authors about some types of materials, experimental systems and methods used in many studies. Here, indicate whether each material, system or method listed is relevant to your study. If you are not sure if a list item applies to your research, read the appropriate section before selecting a response.

Materials & experimental systems

n/a	Involved in the study
☐	☒ Antibodies
☒	☐ Eukaryotic cell lines
☒	☐ Palaeontology and archaeology
☐	☒ Animals and other organisms
☒	☐ Clinical data
☒	☐ Dual use research of concern

Methods

n/a	Involved in the study
☒	☐ ChIP-seq
☒	☐ Flow cytometry
☒	☐ MRI-based neuroimaging

Antibodies

Antibodies used: Mouse anti acetylated-tubulin antibody (Sigma aldrich, Reference# T7451-100UL, Lot# 036M4856V), 1:200 dilution.
Goat anti-mouse IgG (H+L) secondary antibody coupled to Alexa Fluor 647 (Invitrogen, Reference# A21235, Lot#2270554), 1:500 dilution.

Validation: Antibody cross-reactivity against Patiria miniata has been demonstrated in published literature (Annunziata et al., 2013; Carter et al., 2021; Formery et al., 2021)

Eukaryotic cell lines

Policy information about cell lines and Sex and Gender in Research

Cell line source(s)	N/A
Authentication	N/A
Mycoplasma contamination	N/A
Commonly misidentified lines (See ICLAC register)	N/A

Palaeontology and Archaeology

Specimen provenance	N/A
Specimen deposition	N/A
Dating methods	N/A

☐ Tick this box to confirm that the raw and calibrated dates are available in the paper or in Supplementary Information.

Ethics oversight: N/A

Note that full information on the approval of the study protocol must also be provided in the manuscript.

Animals and other research organisms

Policy information about studies involving animals; ARRIVE guidelines recommended for reporting animal research, and Sex and Gender in Research

Laboratory animals	No laboratory animals were used in this study.
Wild animals	Adult Patiria miniata sea stars (age unknown) were collected by scuba diving by a local fishing company (Monterey Abalone Company) in Monterey bay, (CA, USA) following Fish and Game regulations and with appropriate state permitting. Animals were transported in coolers to the marine station and were then kept in tanks with circulating sea water pumped from the bay, and fed with kelp (Macrocystis pyrifera) and commercial seafood until they were used for experiment (RNA tomography) or spawned. After spawning, adult animals used for this study were returned to the tanks and maintained under the same conditions.
Reporting on sex	N/A
Field-collected samples	Field-collected adult Patiria miniata were maintained at sea temperature with natural photoperiod.
Ethics oversight	Animal collection was performed with appropriate state permitting. Handling of echinoderm species is not subject of ethical approvals or restriction in the United States of America.

Note that full information on the approval of the study protocol must also be provided in the manuscript.

Clinical data

Policy information about clinical studies

All manuscripts should comply with the ICMJE guidelines for publication of clinical research and a completed CONSORT checklist must be included with all submissions.

Clinical trial registration	N/A
Study protocol	N/A
Data collection	N/A
Outcomes	N/A

Dual use research of concern

Policy information about dual use research of concern

Hazards

Could the accidental, deliberate or reckless misuse of agents or technologies generated in the work, or the application of information presented in the manuscript, pose a threat to:

No	Yes	
☒	☐	Public health
☒	☐	National security
☒	☐	Crops and/or livestock
☒	☐	Ecosystems
☒	☐	Any other significant area

Experiments of concern

Does the work involve any of these experiments of concern:

No	Yes	
☒	☐	Demonstrate how to render a vaccine ineffective
☒	☐	Confer resistance to therapeutically useful antibiotics or antiviral agents
☒	☐	Enhance the virulence of a pathogen or render a nonpathogen virulent
☒	☐	Increase transmissibility of a pathogen
☒	☐	Alter the host range of a pathogen
☒	☐	Enable evasion of diagnostic/detection modalities
☒	☐	Enable the weaponization of a biological agent or toxin
☒	☐	Any other potentially harmful combination of experiments and agents

ChIP-seq

Data deposition

☐ Confirm that both raw and final processed data have been deposited in a public database such as GEO.

☐ Confirm that you have deposited or provided access to graph files (e.g. BED files) for the called peaks.

Data access links *May remain private before publication.*	N/A
Files in database submission	N/A
Genome browser session (e.g. UCSC)	N/A

Methodology

Replicates	N/A

Sequencing depth	N/A
Antibodies	N/A
Peak calling parameters	N/A
Data quality	N/A
Software	N/A

Flow Cytometry

Plots

Confirm that:

☐ The axis labels state the marker and fluorochrome used (e.g. CD4-FITC).

☐ The axis scales are clearly visible. Include numbers along axes only for bottom left plot of group (a 'group' is an analysis of identical markers).

☐ All plots are contour plots with outliers or pseudocolor plots.

☐ A numerical value for number of cells or percentage (with statistics) is provided.

Methodology

Sample preparation	N/A
Instrument	N/A
Software	N/A
Cell population abundance	N/A
Gating strategy	N/A

☐ Tick this box to confirm that a figure exemplifying the gating strategy is provided in the Supplementary Information.

Magnetic resonance imaging

Experimental design

Design type	N/A
Design specifications	N/A
Behavioral performance measures	N/A

Acquisition

Imaging type(s)	N/A
Field strength	N/A
Sequence & imaging parameters	N/A
Area of acquisition	N/A

Diffusion MRI ☐ Used ☐ Not used

Preprocessing

Preprocessing software	N/A
Normalization	N/A
Normalization template	N/A
Noise and artifact removal	N/A

Volume censoring | N/A

Statistical modeling & inference

Model type and settings | N/A

Effect(s) tested | N/A

Specify type of analysis: ☐ Whole brain ☐ ROI-based ☐ Both

Statistic type for inference (See Eklund et al. 2016) | N/A

Correction | N/A

Models & analysis

n/a	Involved in the study
☐	☐ Functional and/or effective connectivity
☐	☐ Graph analysis
☐	☐ Multivariate modeling or predictive analysis

Functional and/or effective connectivity | N/A

Graph analysis | N/A

Multivariate modeling and predictive analysis | N/A